

**UNDERSTANDING NEURONAL DYNAMICS BY
GEOMETRICAL DISSECTION OF MINIMAL MODELS**

A. Borisyuk¹, J. Rinzel²

¹ *Mathematical Biosciences Institute,
Ohio State University,
Columbus, OH, USA*

² *Center for Neural Science,
New York University,
New York, NY, USA*

Photo: width 7.5cm height 11cm

Contents

1. Introduction	5
1.1. Nonlinear behaviors, time scales, our approach	5
1.2. Electrical activity of cells	6
2. Revisiting the Hodgkin-Huxley equations	10
2.1. Background and formulation	10
2.2. Hodgkin-Huxley gating equations as idealized kinetic models	12
2.3. Dissection of the action potential	13
2.3.1. Current-voltage relations	13
2.3.2. Qualitative view of fast-slow dissection	15
2.3.3. Stability of the fast subsystem's steady states	17
2.4. Repetitive firing	18
2.4.1. Stability of the four-variable model's steady state	18
2.4.2. Stability of periodic solutions	19
2.4.3. Bistability	20
3. Morris-Lecar model	23
3.1. Excitable regime	26
3.2. Post-inhibitory rebound	27
3.3. Single steady state. Onset of repetitive firing, type II	28
3.4. Three steady states	31
3.4.1. Large ϕ . Bistability of steady states	32
3.4.2. Small ϕ . Onset of repetitive firing, Type I	32
3.4.3. Intermediate ϕ . Bistability of rest state and a depolarized oscillation	33
3.5. Similar phenomena in the Hodgkin-Huxley model	35
3.6. Summary: onset of repetitive firing, Types I and II	35
4. Bursting, cellular level	37
4.1. Geometrical analysis and fast-slow dissection of bursting dynamics	38
4.2. Examples of bursting behavior	39
4.2.1. Square wave bursting	39
4.2.2. Parabolic bursting	40
4.2.3. Elliptic bursting	41
4.2.4. Other types of bursting	42
5. Bursting, network generated. Episodic rhythms in the developing spinal cord	44
5.1. Experimental background	44
5.2. Firing rate model	45
5.2.1. Basic recurrent network	45
5.2.2. Full model	46
5.3. Predictions of the model	47
6. Chapter summary	50
6.1. Appendix A. Mathematical formulation of fast-slow dissection.	51
6.2. Appendix B. Stability of periodic solutions.	53
References	55

1. Introduction

1.1. *Nonlinear behaviors, time scales, our approach*

It's been said that the currency of the nervous system is spikes. Indeed, at some level it is important to understand how neurons generate spikes and patterns of spikes. What is their language and how do they convert stimuli into spike patterns? Actually, these are two different questions. The first is about processing and storing information, and a neuron's role in a neural computation. The second is more mechanistic, about the "how" of converting inputs into spike output. With regard to the first, it is rare that we know what neural computation(s) a given neuron carries out, especially since computations more typically involve the collective interaction of many cells. However, we can, as do many cellular neurophysiologists, approach the second question, asking from a more reductionist viewpoint what are the biophysical mechanisms that underlie spike generation and transmission. How do the properties of different ionic channels and their distributions over the cell's dendritic, somatic, axonal membrane determine the neuron's firing modes? How might the various mechanisms be modulated or recruited if there are changes in the cell or circuitry in which it is embedded or in the brain state or in the read-out targets? We usually imagine that the typical time scales for action potential generation are msec, but there are examples of where even a brief (msec) stimulus can evoke a long duration transient spike pattern or where pre-conditioning can delay a spike's onset by 100s of msec. Some neurons fire repetitively (tonically) for steady or slowly changing stimuli, some fire with complex temporal patterns (e.g., bursts of spikes), but some only respond (phasically) to the rapidly changing features of a stimulus. These behaviors reflect a neuron's biophysical makeup.

In these lectures we attempt to describe how different response properties and firing patterns arise. We seek especially to provide insight into the underlying mathematical structure that might be common to classes of firing behaviors. Indeed, the mathematical structure is more general and the physiological implementation could involve different biophysical components. Our approach will be to use concepts from nonlinear dynamics, especially geometrical methods like phase planes or phase space projections from higher dimensional systems. A key feature of our viewpoint is to exploit time scale differences to reduce dimen-

sionality by dissecting the dynamics using fast-slow analysis, i.e., to separately understand the behaviors on the different time scales and then patch the behaviors together. We will begin by dissecting the classical Hodgkin-Huxley model in this way to distinguish the rapid upstroke and downstroke of the spike from the slower behavior during the action potential's depolarized plateau phase and hyperpolarized recovery phase. Analogously we will segregate a burst pattern's active and silent phases from the transitions between these phases. Geometrically, the trajectories during the slow phases are restricted to lower dimensional manifolds and the transitions correspond to reaching folds or bifurcations and jumping to a different manifold where slow flow resumes. Our phase plane treatments will be highlighted in the sections that describe the rich dynamic repertoire of the two-variable Morris-Lecar model, as its biophysical parameters are varied and as we allow them to become slow variables, say, for the generation of bursting behaviors.

For the most part here we will exploit the idealization of a point (i.e., electrically compact) neuron, focusing on the nonlinearities of spiking dynamics, and using biophysically minimal but plausible models. While most of our examples are for single-cell dynamics, the qualitative mathematical structures are also applicable to network dynamics, especially in the mean-field approximations. We work through one such example for network-generated rhythms, as seen in developing neural systems.

A take-home message that will be repeated several times is that the essentials of neural excitability and oscillations are relatively rapid autocatalysis (a regenerative process) and slow negative feedback. At the level of spike generation, say in the Hodgkin-Huxley model: autocatalysis is due to the sodium current's rapid voltage-gated activation while negative feedback comes from sodium inactivation and potassium current activation, both relatively slower. In a network setting autocatalysis could be fast recurrent excitation and negative feedback might be due to intrinsic cellular adaptation or slower synaptic inhibition or depression of excitatory synapses.

1.2. Electrical activity of cells

Electrical activity of a cell is commonly described by the cell's membrane potential (voltage) which can vary between different parts of the cell and also with time. The voltage $V = V(x, t)$ satisfies the current-balance equation:

$$C_m \frac{\partial V}{\partial t} + I_{ion}(V) + I_{coupling} = \frac{d}{4R_i} \frac{\partial^2 V}{\partial x^2} + I_{app}.$$

Here $C_m \frac{\partial V}{\partial t}$ is current due to the membrane's capacitive property, $I_{ion}(V)$ represents the cell's intrinsic ionic currents, $I_{coupling}$ represents the inputs and in-

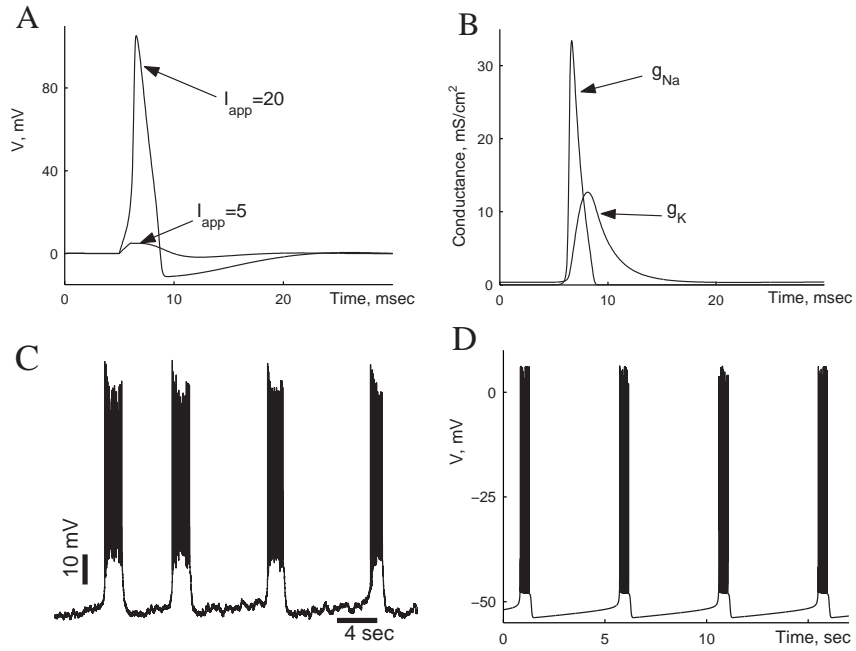


Fig. 1. Modes of neuronal activity. *A-B*: Excitability in response to a brief current pulse (Hodgkin-Huxley model, same as in section 2, pulse duration 1 msec). *A*: Pulse of amplitude $I_{app} = 5 \mu\text{A}/\text{cm}^2$ fails to induce a spike, voltage returns to rest. Pulse of amplitude $I_{app} = 20 \mu\text{A}/\text{cm}^2$ elicits a single spike. *B*: time courses of Na^+ and K^+ conductances during the spike from *A*. *C-D*: Single neuron bursting in brain stem circuit involved with respiration. *A*: Voltage recording in rat. Data courtesy of Christopher A. Del Negro and Jack L. Feldman. See also, Figure 1 of [5]. *B*: Voltage trace in a model. Equations used are the same as in [5], with $I_{app} = 0 \mu\text{A}/\text{cm}^2$, $g_{syn} = 0 \text{ mS}/\text{cm}^2$, $g_{ton} = 0.3 \text{ mS}/\text{cm}^2$.

teraction currents from coupling with other cells (with their voltages, V_j), while I_{app} is the current supplied by the experimentalist's electrode. The term $\frac{\partial^2 V}{\partial x^2}$ represents current spread along dendritic or axonal segments due to spatial gradients in voltage (d is diameter, R_i is cytoplasmic resistivity). We will neglect this term by considering the case of a "point" neuron, i.e. all the membrane currents and inputs are lumped into a single "compartment" with V independent of x . This can be a good approximation when the cell is electrically compact.

Coupling to other cells can be via chemical synapses. Neurotransmitter released from the presynaptic cell " j " activates receptors on the postsynaptic membrane that in turn open channels, allowing for the flow of some types of ions:

$$\sum_j g_{syn,j}(V_j(t))(V - \bar{V}_{syn}).$$

In fact, $g_{syn,j}$ is not really an instantaneous function of V_j and its dynamics can be quite important, although we will not be addressing these issues here. Coupling may also be "electrical" mediated by gap junctions (formed by local clusters of ionic channels that span the abutting membranes of both cells), that act effectively as resistors:

$$\sum_j g_{elec,j}(V - V_j).$$

The term I_{ion} includes all of the intrinsic ionic currents present in the cell,

$$I_{ion} = \sum_k g_k(V - \bar{V}_k).$$

Although approximately Ohmic instantaneously, these currents provide significant nonlinearities. Their conductances g_k are voltage-dependent and dynamic, expressed in terms of gating variables with a variety of time scales from msec to 10s or 100s of msec. Sometimes conductances are also affected by the presence of various substances, for example, by concentrations of other ions, second messengers, etc. The reversal potential \bar{V}_k for current flow depends on the ionic channels' (of " k " type) selectivity for ions. The most common ionic species contributing to the electrical activity are Ca^{2+} , Na^+ , K^+ , and Cl^- . There are several different types of channels associated with each of these various ions, and some channels pass more than one type of ion.

The available constellation of different channel types leads to a large variety of nonlinear properties and electrical activity patterns amongst cells, even in the absence of coupling. The simplest example of a cell's nonlinear responsiveness is the generation of a spike or action potential. After stimulation by a small brief

pulse of I_{app} V returns back to rest, quite directly (Fig. 1A). However, if the stimulus exceeds a threshold value, V executes a large and characteristic excursion (action potential) and then eventually returns to rest (Fig. 1A). Briefly, the events are as follows (Fig. 1B). Note first that according to the current balance equation, V will tend toward the \bar{V}_k associated with the momentarily dominant g_k . Thus, the spike's regenerative upstroke (for example, in the Hodgkin-Huxley model, see section 2) is due to the rapid V -dependent increase in g_{Na} pushing V toward \bar{V}_{Na} . Then also driven by V but on a slower time scale, g_{Na} turns off while g_K activates, pushing V toward \bar{V}_K . The fall in V causes g_K to eventually die down and the system returns to rest. Excitability involves fast autocatalysis (V rises opening Na^+ channels causing V to increase further, etc) and slower negative feedback (g_{Na} shuts down and g_K turns on). Non-linearity is manifested also in the fact that the spike's amplitude is approximately independent of stimulus strength, provided it is superthreshold. Many models and cells respond to a step of I_{app} by firing repetitively. The firing frequency typically exhibits a transient phase and may then adapt to a steady level. The adapted firing frequency (f) versus I_{app} is a typical characterization of the cell or model's input-output relation ($f - I$ curve) (e.g., Fig. 5B). How the $f - I$ curve's shape, position, and frequency range depend on state parameters or background activity are of interest. In cells that show bursting behavior (Fig. 1C,D) a much slower negative feedback (for example, a slowly activating K^+ current) can bring the cell out of firing mode. Then, during the long quiescent phase, while V is low the negative feedback process recovers and re-entry into the firing mode occurs eventually. Other instances of nonlinear behavior involve various types of bistability, exhibited by some neurons. A cell might be either quiescent or firing repetitively for a steady stimulus or maybe capable of firing at two different frequencies (a multi-valued $f - I$ curve). Without intervention each state might persist for 100s of msec. The cell can be switched from one state to the other by brief stimuli.

In some experimental situations V can be measured directly with an electrode, by penetrating or attaching it to the cell (this is much easier to do *in vitro* than *in vivo*). This yields $V(t)$ at one site (typically, the soma) that may or may not reflect what is happening in other parts of the cell, in particular along the axon, which carries the output signal to other areas. While much theoretical research has been done on spatial characteristics, such as action potential propagation (see, e.g. [54, 55]) and the role of dendrites (for reviews see, e.g., [47, 48, 60, 61]), in this chapter we will focus on the point neuron.

2. Revisiting the Hodgkin-Huxley equations

2.1. Background and formulation

Before we analyze mathematically action potential generation, let's review the experimental basis and determination of the equations. The recipe for experimentally describing the currents that dictate neuronal electric properties comes from the work of Hodgkin and Huxley ([35] and, for reviews, [33, 38, 52]). Two major hurdles were overcome. First, in order to isolate I_{ion} , the confounding and unknown contribution from the spatial spread of current had to be eliminated. Hodgkin and Huxley chose to use the squid's giant axon [35], extracted and isolated in a dish. It is so big that one can insert a silver wire along its length. Because silver is a good conductor, it equalizes voltage values along the observable segment, constituting the so-called "space-clamp". Second, to dissect the contributions of individual ionic currents one can eliminate some of the ionic species from the bathing solution, thereby revealing the membrane current contributed by other ions. Finally, a tour de force: the voltage-clamp technique involves a feedback circuit to deliver the appropriate current to the axon so that V is held fixed to a commanded level. By systematically using different command V 's the dynamics and V -dependence of the isolated current can be found. Another use of the voltage-clamp technique is to zero out the contribution of the k type current by clamping V to \bar{V}_k , recalling that \bar{V}_k (the Nernst potential) can be altered by changing ion concentrations in bath or axon. After the ionic current time courses are measured they can be empirically fitted with solutions of differential equations.

With the V -dependent kinetics of different contributing ionic currents in hand, the test phase involves combining them along with the capacitive membrane current to thus synthesize the current-balance equation. Then, by numerical integration, confirm that the constituted equations describe the evolution of V as a function of I_{app} (i.e., under current-clamp).

Hodgkin and Huxley shared a Nobel prize for their description of I_{ion} , accounting for the action potential in squid giant axon and for providing the framework for other excitable membrane systems. Fortunately, there were only two voltage-gated currents, for Na^+ and for K^+ , the delayed-rectifier K^+ current, and a constant-conductance leak current. The equations (space-clamped configuration) are:

$$\begin{aligned}
 C_m \dot{V} &= -I_{ion}(V, m, h, n) + I_{app} \\
 &= -\bar{g}_{Na} m^3 h (V - \bar{V}_{Na}) - \bar{g}_K n^4 (V - \bar{V}_K) - g_L (V - \bar{V}_L) + I_{app}, \\
 \dot{m} &= \phi [m_\infty(V) - m] / \tau_m(V), \\
 \dot{h} &= \phi [h_\infty(V) - h] / \tau_h(V),
 \end{aligned} \tag{2.1}$$

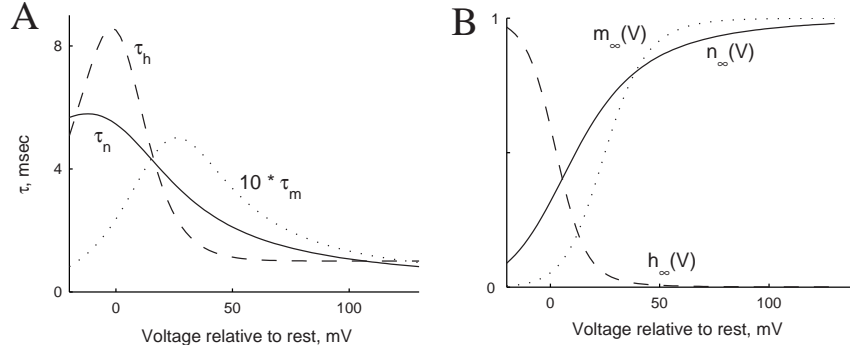


Fig. 2. Functions $\tau_x(V)$ (in A) and $x_\infty(V)$ (in B) in Hodgkin-Huxley equations 2.1 for m (dotted), n (solid) and h (dashed). Notice that $\tau_m(V)$ was multiplied by 10 for plotting on the same scale.

$$\dot{n} = \phi [n_\infty(V) - n] / \tau_n(V),$$

where membrane potential V is in mV, and expressed relative to rest; t is in msec; m , h and n are the dimensionless phenomenological gating variables (with values between 0 and 1): sodium activation, sodium inactivation, and potassium activation. The applied current I_{app} ($\mu\text{A}/\text{cm}^2$) will be taken as time-independent in this section. The functions $\tau_x(V)$ and $x_\infty(V)$ can be interpreted as, respectively, the “time constant” and the “steady-state” functions for m , h , n . Their graphs are shown in Figure 2. The activation variables have steady-state functions that increase with V and asymptote to 1, while for the inactivation variable $h_\infty(V)$ decreases with V and asymptotes to 0. Note also in Fig. 2 that the time constant scale for m is about 1/10 that for h and n , so that m is relatively fast. The temperature factor ϕ speeds up the rates for m , h , n for increasing temperature with Q_{10} of 3:

$$\phi = 3^{(\text{Temp}-6.3)/10}.$$

Here, we fix the temperature at 18.5°C , unless noted otherwise. Values for the other parameters are as in the original model (see, e.g. [38]).

After these many years, the conceptual approach of Hodgkin and Huxley (voltage-clamp, segregate currents, synthesize and confirm) and general form of the mathematical expressions for conductances (products of gating variables) are still being widely applied. Many cell types, with different types of currents, have been successfully studied experimentally, and described in models using the same framework. Some examples include [33, 38, 39] Ca^{2+} currents (I_{Ca} ; T,L,N types), A-current (I_A ; K^+ current with inactivation), Ca^{2+} -dependent K^+ current (I_{K-Ca} ; K^+ current activated by voltage and intracellular Ca^{2+} concentration).

These advances are aided by development of new experimental techniques [33]. For example, to reduce the complexity of the system the ionic channels can be selectively blocked by pharmacological agents or disabled by genetic modification; the patch-clamp recording technique gives accurate access to currents and channels in electrically compact neurons or even a small patch of membrane, sometimes containing only a single channel whose opening/closing statistics are then obtained.

From the modeling perspective, it is important to keep in mind that even though many of the ionic currents can be described in the Hodgkin-Huxley formalism, and written in the form of equations 2.1, the parameters can be difficult to measure experimentally. In fact, it is rare that the voltage-clamp data are available for all channel types that are present in a given neuronal system. For example, the time constants of activation and inactivation of currents are often hard to measure. Therefore, the parameters in the model have to be estimated from empirical observations and indirect measurements. Also, in developing a model, the parameters of a particular channel are sometimes borrowed from other experimental systems where the channel has been studied in more detail. This latter technique has to be used with caution — there are many different types of channels for each ionic species, and their dynamics often differs significantly, so one model cannot always be substituted to describe other types of channels for the same ion.

2.2. Hodgkin-Huxley gating equations as idealized kinetic models

In this section we outline an interpretation of the Hodgkin-Huxley gating variables in terms of idealized kinetic schemes, but these schemes are not meant as realistic representations of a channel's molecular dynamics. In particular, the “gating subunits” in the Hodgkin-Huxley model (see below) are not the molecular subunits of the channel conformation. For an introduction to the molecular biology of ionic channels see, e.g., [33]. The representation here treats activation and inactivation as independent, and each gating subunit obeys a one-step kinetic scheme.

Each of the quantities m, h, n can be interpreted as a probability for a specific gating subunit to be “available”. In this interpretation a Na^+ channel is said to consist of 3 “ m -subunits” and 1 “ h -subunit”, and a K^+ channel has 4 “ n -subunits”. If all gating subunits must be available to open a channel, and the subunits are independent, then the probability of the channel to be open is the product of probabilities of the subunits to be available. Further, the total conductance of the channels of a given type is proportional to the fraction of channels open, which, in turn, is proportional to the probability of the channel being open if the number of channels is large. Hence, say, for the K^+ current the

instantaneous conductance is n^4 , and the coefficient of proportionality, \bar{g}_K (say, mS/cm²) is the maximal conductance if all channels are open, i.e. \bar{g}_K equals the local channel density times the conductance of a single open channel.

For the dynamics of a gating subunit of type x suppose the subunit has only 2 states: “available” and “unavailable”, and the rate of going from unavailable to available is $\alpha_x(V)$ and from available to unavailable is $\beta_x(V)$. Notice that the rates are voltage-dependent. Then the probability (or fraction) of available subunits, x , satisfies

$$\dot{x} = \alpha_x(V)(1 - x) - \beta_x(V)x.$$

Dividing both sides of this equation by $\alpha_x(V) + \beta_x(V)$, and introducing notations $\tau_x(V) = 1/(\alpha_x(V) + \beta_x(V))$ and $x_\infty(V) = \alpha_x(V)/(\alpha_x(V) + \beta_x(V))$, we get

$$\tau_x(V)\dot{x} = x_\infty(V) - x,$$

which has the same form as in Hodgkin-Huxley equations 2.1.

2.3. Dissection of the action potential

To understand the dynamics of action potential generation (figure 3A) we will use the fact that there are two different time scales in the system; τ_m is much smaller than τ_h and τ_n (see Figure 2A). Using the methods of fast-slow analysis we dissect the system into fast (for V, m) and slow (for n, h) subsystems. In fact, m is so fast that we will treat it as instantaneous for now, setting $m = m_\infty(V)$, and thus the fast subsystem is one-dimensional. Here, we describe the process in mixed mathematical and biophysical terms; a more formal description of the framework is in Appendix A.

2.3.1. Current-voltage relations

Motivated by the biophysicist’s interest in the membrane’s current-voltage relations we will examine these on two different time scales. First, we consider the steady current that is needed to maintain a constant voltage (as in voltage-clamp). This steady state current, $I_{ss}(V)$, equals $I_{ion}(V, m, h, n)$ with all gating variables set to their steady state values:

$$\begin{aligned} I_{ss}(V) &= I_{ion}(V, m_\infty(V), h_\infty(V), n_\infty(V)) \\ &= \bar{g}_{Na}m_\infty^3(V)h_\infty(V)(V - \bar{V}_{Na}) + \bar{g}_Kn_\infty^4(V)(V - \bar{V}_K) + \bar{g}_L(V - \bar{V}_L). \end{aligned}$$

Figure 3B shows the steady-state current for each type of ion and the total I_{ss} for equations 2.1. Notice that for the Hodgkin-Huxley equations this current is monotonically increasing. It is dominated by the steadily-activated K^+ -current.

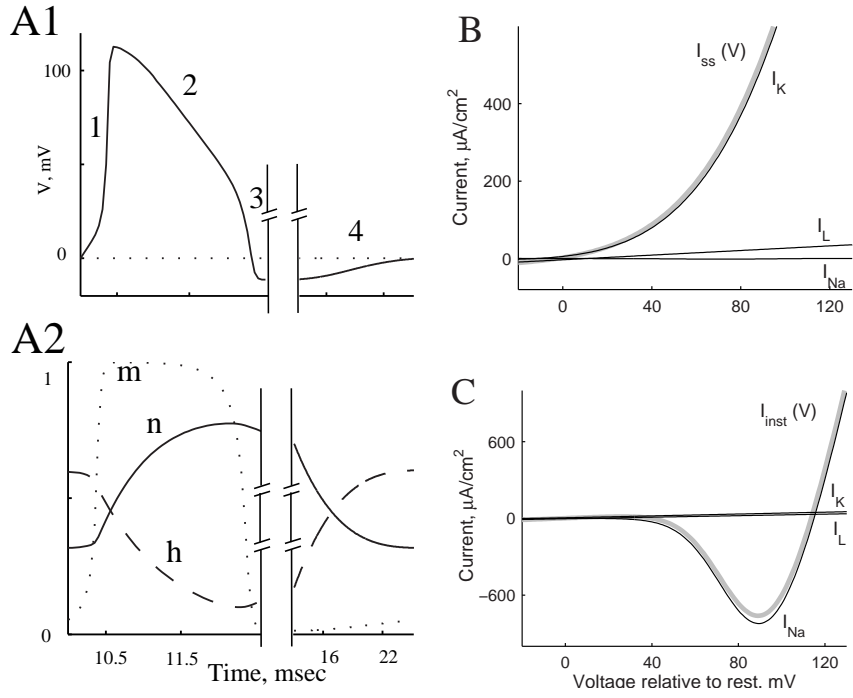


Fig. 3. Illustration of the Hodgkin-Huxley equations. *A*: Time courses of voltage (*A1*) and gating variables (*A2*) during an action potential. Notice that time scale is compressed at the second part of the graph to include the recovery phase. Numbers in the upper panel denote different phases of the action potential (see text). Stimulus is a step of current delivered at $t = 10\text{msec}$ of duration 1 msec and with amplitude $I_{app} = 20\mu\text{A}/\text{cm}^2$. *C*: Steady state currents for each ionic type (black) and total $I_{ss}(V)$ (grey). *D*: Instantaneous currents each ionic type (black) and total $I_{inst}(V)$ (grey).

I_{Na} plays little role in $I_{ss}(V)$ because of inactivation; $m_\infty(V)$ and $h_\infty(V)$ "overlap" only slightly.

Second, on a very short time scale the instantaneous current, $I_{inst}(V)$, describes the V -dependence of $I_{ion}(V, m, h, n)$ with $m = m_\infty(V)$ and with n and h frozen, since they are so slow (on this time scale):

$$\begin{aligned} I_{inst}(V; n_0, h_0) &= I(V, m_\infty(V), h_0, n_0) \\ &= \bar{g}_{Na} m_\infty^3(V) h_0 (V - \bar{V}_{Na}) + \bar{g}_K n_0^4 (V - \bar{V}_K) + \bar{g}_L (V - \bar{V}_L). \end{aligned}$$

When n and h are fixed at their rest values $I_{inst}(V)$ approximates the net ionic current that will be produced if the membrane potential is quickly perturbed from rest to the value V . Figure 3C shows this current, as a function of V , for equations 2.1 with n and h fixed at rest values.

2.3.2. Qualitative view of fast-slow dissection

Here, using the current-voltage relations defined in the previous section, we can describe a Hodgkin-Huxley action potential (Fig. 3A). Except for a brief initial transient pulse we will assume that $I_{app} = 0$ in this section.

We idealize the action potential as consisting of 4 phases (see Figs. 3A and 4): (1) upstroke, (2) plateau, (3) downstroke, and (4) recovery. The upstroke and downstroke happen on the fast time scale. Therefore we will use the approximation that the slow variables h and n are constant during these phases, so that V satisfies

$$C_m \frac{dV}{dt} = -I_{inst}(V; n_0, h_0). \quad (2.2)$$

The plateau and recovery, on the other hand, happen on the slow time scale. During these two phases the dynamics is determined by h and n , whereas V and m are "slaved", or "equilibrated": their values follow the dynamics of h, n in such a way that the right-hand sides of their equations remain zero:

$$0 = -I(V, m_\infty(V), h, n) = -I_{inst}(V, h_0, n_0).$$

Note, this does not mean that $dV/dt = 0$ but rather that that V is so fast that it can be treated as tracking instantaneously a zero of $I_{inst}(V, h, n)$.

Upstroke (phase 1, characterized by the very rapid activation of Na^+ channels, Figure 4 *top left*): assume h, n are slow (fixed at their rest values); m instantaneous ($m = m_\infty(V)$), V satisfies 2.2. This a one-dimensional dynamical system and its dynamics is determined by the zeros and signs of the right hand side of the equation 2.2. The graph of $I_{inst}(V)$ is N-shaped, therefore there are 3 steady states (R,T,E) (see Fig. 4), corresponding to *Rest*, *Threshold* and *Excited* states. We show in the section 2.3.3 below that their stability is determined by the sign

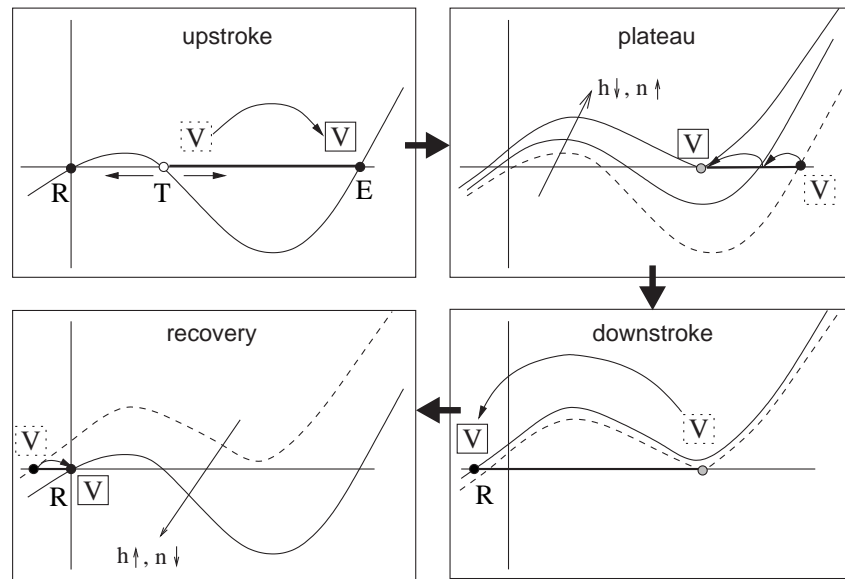


Fig. 4. Phases of Hodgkin-Huxley action potential shown in the $V - I_{inst}$ plane (see text). In each panel the dashed curve is the position of $I_{inst}(V)$ at the beginning of the phase, and V in dashed square marks the initial value of V . Solid curve and label are the curve and V -value at the end of the phase. Arrows above the x-axis show the motion of V , and arrows below axis in the first panel show the direction of flow for V . R , T , E denote rest, threshold and excited steady states, respectively.

of the derivative $\frac{dI_{inst}}{dV}$, and that R and E are stable, and T is unstable. If V is depolarized above T, it increases on the fast time scale toward E (Figure 4 top left).

Plateau (phase 2, Figure 4 top right): as V reaches E (depolarizes), the slow dynamics for h and n take place. The solution remains at $I(V, m_\infty(V), h, n) = 0$, but this curve as a function of V is parameterized by h and n and these parameters are changing according to their dynamics 2.1. For depolarized V : h decreases, n increases, i.e. the (positive) contribution of K^+ current increases and the negative feedback contribution of Na^+ inactivation decreases I_{Na} . Therefore, the N-shaped curve of $I(V; h, n)$ drifts upward. As a result the steady states T and E move closer together until they coalesce and disappear, ending phase 2 (Figure 4 top right).

Downstroke (phase 3, Figure 4 bottom right): now there is only one steady state (hyperpolarized R) and V decreases toward it (on the fast time scale).

Recovery (phase 4, Figure 4 bottom left): In this phase V is hyperpolarized. Therefore, h increases and n decreases. As a result I_{inst} slowly moves downward; R returns to the original value and V drifts with it.

2.3.3. Stability of the fast subsystem's steady states

Now, for the analysis of the action potential it remains to show that the stability of any steady state V_{ss} of the equation

$$C_m \frac{dV}{dt} = -I_{inst}(V, m_\infty(V), h_0, n_0) + I_{app} = -I_{inst}(V; n_0, h_0) + I_{app}$$

is determined by the derivative of the right-hand side.

Consider the effect of a small perturbation v from the steady state $V(t) = V_{ss} + v(t)$. Then

$$\begin{aligned} C_m \frac{dV}{dt} &= C_m \frac{dv}{dt} = -I_{inst}(V_{ss} + v; n_0, h_0) + I_{app} \\ &= -I_{inst}(V_{ss}; n_0, h_0) - \left. \frac{dI_{inst}}{dV} \right|_{V_{ss}} v + O(v^2) + I_{app}. \end{aligned}$$

The first and last terms sum to 0, because V_{ss} is a steady state. As a linear approximation, we have:

$$C_m \frac{dv}{dt} = - \left. \frac{dI_{inst}}{dV} \right|_{V_{ss}} v.$$

The steady state is

$$\text{stable if } \left. \frac{dI_{inst}}{dV} \right|_{V_{ss}} > 0,$$

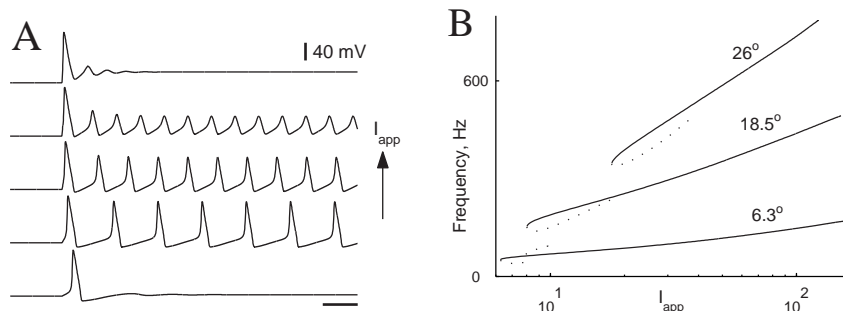


Fig. 5. Repetitive firing through Hopf bifurcation in Hodgkin-Huxley model. A: Voltage time courses in response to a step of constant depolarizing current (several levels of current: from bottom to top: $I_{app} = 5, 15, 50, 100, 200$ in $\mu\text{amp}/\text{cm}^2$). Scale bar is 10 msec. B: f-I curves for temperatures of 6.3, 18.5, 26°C, as marked. Dotted curves show frequency of the unstable periodic orbits.

and

$$\text{unstable if } \left. \frac{dI_{inst}}{dV} \right|_{V_{ss}} < 0.$$

A biophysical interpretation for this instability condition is that negative resistance, due to the rapidly activating I_{Na} , is destabilizing.

2.4. Repetitive firing

Numerical simulations show that the Hodgkin-Huxley model exhibits repetitive firing in response to steady I_{app} within a certain range of values, $I_\nu < I_{app} < I_2$ (Fig. 5 A) [15, 57]. Generally, the firing rate increases and the amplitude of spikes decreases with increasing current. If I_{app} is too large V settles to a stable depolarized level. This is called depolarization block. As the temperature is increased the frequency range moves upward (Fig. 5 B). This is because the recovery processes h and n become faster and the membrane's refractory period decreases. However, if the temperature is increased too much then excitability and repetitive firing is lost, i.e. the negative feedback is too fast. In order to study the emergence and properties of rhythmic behavior we use stability and bifurcation theory.

2.4.1. Stability of the four-variable model's steady state

The Hodgkin-Huxley model has a unique steady state voltage V_{ss} for each value of I_{app} , because I_{ss} is monotonic. Yet we see that for some levels of I_{app} the membrane oscillates and does not remain stably at V_{ss} . To find the conditions for

stability of the steady state, we linearize the full system 2.1 around

$$(V_{ss}, m_{\infty}(V_{ss}), h_{\infty}(V_{ss}), n_{\infty}(V_{ss})).$$

This leads to the constant coefficient 4th order system for evolution of the vector $y(t)$ of perturbations of (V, m, h, n) :

$$\frac{dy}{dt} = J_{ss}y,$$

where J_{ss} is the 4x4 Jacobian matrix of 2.1, evaluated at the steady state. The four eigenvalues λ_i of J_{ss} determine stability. Stability requires that each λ_i have negative real part. If any of them has positive real part then the steady state is unstable. In Fig. 6A we plot the leading eigenvalues as functions of I_{app} . Indeed, we have stability for low and high values of I_{app} . However, there is an intermediate range of I_{app} : $I_1 < I_{app} < I_2$ where the steady state point is unstable. The leading eigenvalues form a complex pair and the steady state loses stability via a Hopf bifurcation [30, 62] as I_{app} increases through the critical value I_1 and regains stability via Hopf bifurcation as I_{app} increases through I_2 . Figure 7A shows V_{ss} as a function of I_{app} (thin lines). (Note, this is just a replotting of I_{ss} from Fig. 3B.) The values I_1 and I_2 depend on temperature and other parameters of the system. Figure 7B shows how the region of instability shrinks with temperature. As the numerical simulations suggest the model oscillates stably for $I_1 < I_{app} < I_2$ and rhythmicity is lost at high temperature [49, 57]. The branches for $I_1(Temp)$ and $I_2(Temp)$ coalesce at $Temp = 28.85^\circ\text{C}$. Notice, there are no Hopf bifurcations, and the steady state does not lose stability above this temperature.

2.4.2. Stability of periodic solutions

The theory of Hopf bifurcations [30, 62] guarantees that small amplitude oscillations emerge at the critical I_{app} values. In this Hodgkin-Huxley case, the bifurcation is subcritical at I_1 (unstable oscillations on a branch directed into the region where the steady state is stable) and supercritical at I_2 . One could compute these local properties by evaluating complicated expansion formulae [30]. Alternatively, the emergence, extension to large amplitude and stability of these periodic solutions, both stable and unstable orbits, can be traced across a range of parameters, using a variety of numerical methods (e.g. [18, 57]). Such branch tracking software [18] was used to compute the periodic solutions as a function of I_{app} , shown in Figure 7A (thick lines).

The stability of a periodic solution, in general, is determined according to the Floquet theory [10, 30, 71]. We describe this formally in Appendix B and here just sketch the idea and give the numerical results from the stability analysis. In

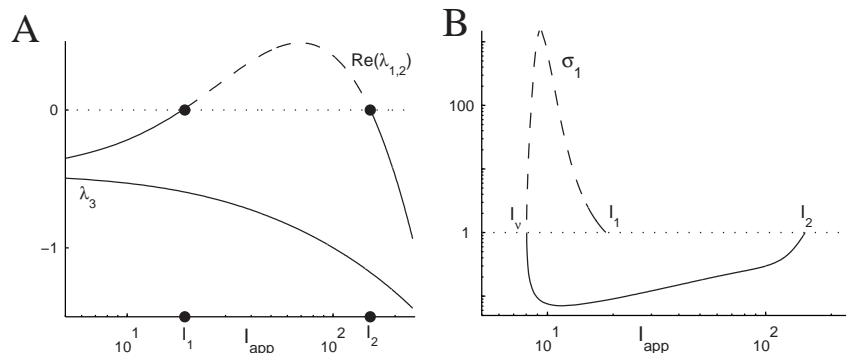


Fig. 6. Stability of steady states and periodic orbits in the Hodgkin-Huxley model. *A*: Real part of the complex pair of eigenvalues $Re(\lambda_{1,2})$ and third negative eigenvalue λ_3 . λ_4 is even more negative is off the scale of this plot. For $I_1 < I_{app} < I_2$ $Re(\lambda_{1,2})$ is positive (dashed), showing instability of the steady state. *B*: Values of the leading non-trivial Floquet multiplier along the branch of periodic solutions in log-log axes. The part of the curve with $\sigma_1 > 1$ (dashed) indicates instability of the periodic solutions (see text). In both panels I_{app} is in $\mu A/cm^2$.

analogy to the steady state case, we linearize the equations 2.1 about the periodic solution (period T),

$$\frac{dy}{dt} = J_{osc}y,$$

where J_{osc} , the 4x4 Jacobian matrix, now has entries that are periodic. It has solutions of the form $exp(\lambda t)q(t)$ where q is periodic. The cycle-to-cycle growth or decay of perturbations are governed by the numbers $\sigma = exp(\lambda T)$, the Floquet multipliers. If any σ (of the 4) has $|\sigma| > 1$ then the periodic solution is unstable. The (nontrivial) leading multiplier σ_1 is plotted vs. I_{app} in Fig. 6B along the branch of periodic solutions. (Note, there is always one σ equal to unity since the derivative of the periodic solution satisfies the above linear equation, with $\lambda=0$.) The curve is multivalued because for $I_\nu < I_{app} < I_1$ two periodic solutions exist, one stable (corresponding to repetitive firing) and one unstable. The leading Floquet multiplier is greater than 1 for the unstable orbit (thick dashes), in fact much larger than 1, indicating that this orbit would not be seen in forward integration of 2.1 and, even more unlikely, in experiments.

2.4.3. Bistability

Notice that for a range of applied current, $I_\nu < I_{app} < I_1$, the stable steady state and the stable limit cycle coexist. This means that the system is bistable, i.e. that for the same value of parameters depending on initial conditions the long-term state of the system can be different. In this section we discuss predictions of the

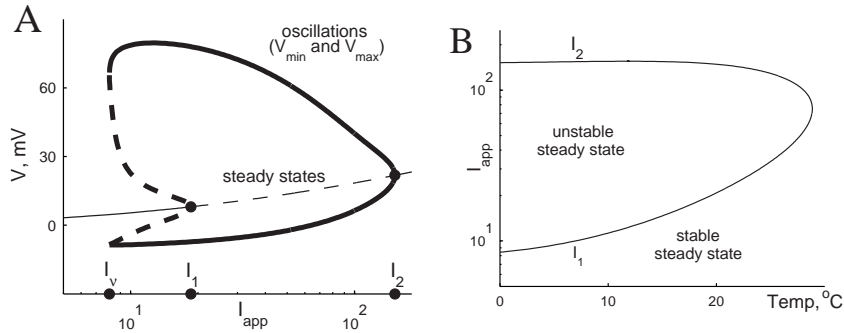


Fig. 7. A: Bifurcation diagram showing the possible behaviors for the Hodgkin-Huxley equations for different values of I_{app} at temperature 18.5°C . I_1 and I_2 denote Hopf bifurcations of the steady states, I_ν bifurcation of the periodic solutions. *Thin solid curves*: stable steady state, *thin dashed curves*: unstable steady state, *thick solid curves*: maximum and minimum V of the stable limit cycle, *thick dashed curves*: maximum and minimum V of the unstable limit cycle. B: Range of I_{app} where the steady state is unstable plotted as a function of temperature. In both panels I_{app} is in $\mu\text{A}/\text{cm}^2$.

model derived from the existence of bistability and their experimental verification for the squid giant axon.

One prediction concerns the onset of repetitive firing. The model predicts two critical values of current intensity for the onset of repetitive firing (Fig. 7A): a lower one (I_ν) for a suddenly applied stimulus, and an upper one (I_1) for a slowly increasing ramp. The reason for this is that if the system starts at the steady state and the applied current is below I_ν , then gradual increase of current will keep the solution at the stable steady state until it loses stability at I_1 . On the other hand, if a current is turned on abruptly above I_ν , then the phase space abruptly changes to include the stable limit cycle and the system may find itself in the domain of attraction of the limit cycle. Experimentally determining both critical values for the onset of repetitive firing also indicates the range of currents (between the critical values) where bistability is expected.

A second prediction is that if I_{app} is tuned into the range for bistability, then brief perturbations of appropriate strength and phase will stop the repetitive firing. Moreover, the model predicts that such annihilation can be evoked by depolarizing as well as hyperpolarizing perturbations. This prediction is based on the fact that the domains of attraction are separated by a surface (which presumably contains the unstable limit cycles mentioned above (see [49, 57])). This structure suggests that the trajectory could be forced across the separatrix surface by a brief perturbation. In Hodgkin-Huxley simulations by Cooley et al. [15] and in experiments with stretch receptors of Gregory et al. [29] it was shown that a neural system can be shocked out of the steady state into repetitive firing. Later

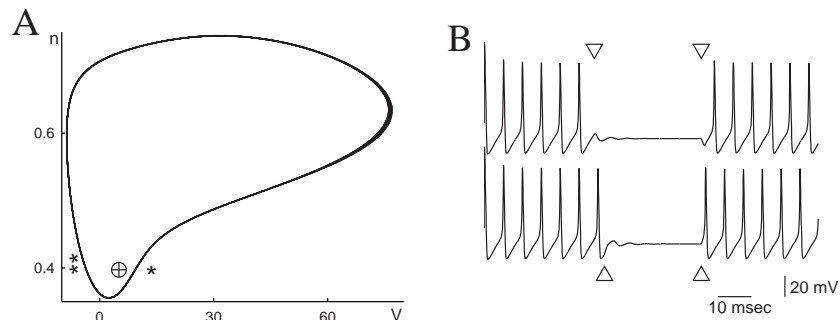


Fig. 8. Bistability in the Hodgkin-Huxley equations ($I_{app} = 9 \mu\text{A}/\text{cm}^2$) A: Projection from 4-dimensional phase space onto the $V - n$ plane. Projections of stable periodic orbit and stable fixed point are shown. Also marked are the phases of the limit cycle where hyperpolarizing (asterisk) or depolarizing (double asterisk) perturbations may switch the system to the domain of attraction of the steady state. B: Time courses of V with continuous spiking that is stopped by a delivery of a short pulse of current. Upper: hyperpolarizing pulses of current delivered at $t = 33$ msec (strength $-5 \mu\text{A}/\text{cm}^2$), and $t = 65$ msec (strength $-10 \mu\text{A}/\text{cm}^2$); lower: depolarizing pulses at $t = 36$ msec (strength $5 \mu\text{A}/\text{cm}^2$) and $t = 65$ msec (strength $10 \mu\text{A}/\text{cm}^2$). All pulses are square shaped current injections of duration 1. Initial conditions: $V_0 = 20\text{mV}$, $m = 0.6$, $h = 0.6$, $n = 0.45$.

Guttman et al. [32] demonstrated both theoretically and experimentally that the Hodgkin-Huxley system and squid giant axon can be shocked out of the periodically spiking state. To choose the appropriate phase and amplitude of the perturbation it is useful to look at the projection of the 4-dimensional phase space to a 2-dimensional plane. Figure 8A shows the stable limit cycle and the stable fixed point in the $V - n$ plane. This graph indicates that if we have a trajectory running along the limit cycle, and we deliver a hyperpolarizing perturbation just before the upstroke of the action potential (marked with an asterisk) or a depolarizing perturbation at the end of the recovery period (marked with two asterisks), then it is possible to switch the trajectory into the domain of attraction of the fixed point. The system will stop firing and will exhibit damped oscillations to the steady state (see examples in Fig. 8B). It is important to remember that the two-dimensional projection of the phase space in Figure 8A does not give an accurate picture of the behavior of the solutions. In the $V - n$ plane trajectories can cross while this is ruled out for the actual four-dimensional trajectories. Moreover, the perturbations that bring trajectories close to one of the attractors in the plane do not necessarily bring the actual trajectory across the separating surface. Therefore we treat two-dimensional projections as merely a useful indication of the behavior of the full system.

The model also indicates that it may be easier to stop periodic firing if the bias

current is just above I_ν , and it is easier to start the oscillation if the bias current is closer to I_1 , because the domain of attraction of the fixed point is reduced near I_1 .

Most of these predictions were qualitatively confirmed experimentally in the squid axon preparation [32]. Squid giant axon bathed in low Ca^{2+} can exhibit co-existent stable states, one oscillatory (repetitive firing) and one time-independent (steady-state), for just superthreshold values of the applied current step. For a slow up and down current ramp the critical current intensities for switching from one stable to other depend on whether current was increasing or decreasing. That is, the experimental system manifests a hysteresis behavior in this near threshold region. Moreover, repetitive firing in response to a just-superthreshold step of current was annihilated by a brief perturbation provided its amplitude and phase were in an appropriate range of values.

The existence of a range of bistability has important implications for overall dynamics of the system. First, it allows greater stability in the near-threshold regime in the presence of noise. This is the same principle as used in thermostats — once the system is settled to one of the stable states small perturbations have little effect. Bistability in the system can also underlie more complex firing patterns in the autonomous system — for example, it can provide the basis for bursting, observed in many cell types (see section 4). To achieve this, the bifurcation parameter (I_{app} in our case) becomes a dynamic variable whose typical time scale is much longer than the typical oscillation period. Finally, we note that similar phenomena can occur if other quantities are used instead of I_{app} as bifurcation parameters (or as slow dynamic variables), for example the concentration of intracellular Ca^{2+} .

3. Morris-Lecar model

In order to more fully exploit the power of geometric phase-plane analysis and bifurcation theory in understanding neuronal dynamics we focus on a two-variable model of cellular electrical activity. The model was developed by Morris and Lecar in 1981 [40] in their study of barnacle muscle electrical activity and then popularized as a reduced model for neuronal excitability [53]. Our presentation parallels some of that in [53]. The Morris-Lecar model is formulated in the Hodgkin-Huxley framework, with biophysically meaningful parameters and structure, yet it is simple enough to analyze and it exhibits a great repertoire of interesting behaviors (see e.g. [53]). Of course, it is rather idealized compared to many other neuronal models that are designed to investigate the details of interaction of many known ionic currents, or the spatial propagation of activity, etc. Such minimal models however are invaluable when the problem or questions at

hand require only qualitative or semi-quantitative characterizations of spiking activity. This is especially important in studies of large networks of cells. We note that the geometrical approach via phase plane analysis was pioneered in the study of neuronal excitability by Fitzhugh [22, 23].

The Morris-Lecar model incorporates a delayed-rectifier K^+ current similar to the Hodgkin-Huxley I_K and a fast non-inactivating Ca^{2+} current (depolarizing, and regenerative, like the Hodgkin-Huxley I_{Na}). The activation of Ca^{2+} is assumed to be so fast that it is modeled as instantaneous. The model equations are

$$\begin{aligned} C \frac{dV}{dt} &= -I_{ion}(V, w) + I_{app} \\ &= -(\bar{g}_{Ca} m_\infty(V)(V - \bar{V}_{Ca}) + \bar{g}_K w(V - \bar{V}_K) + \bar{g}_L(V - \bar{V}_L)) + I_{app}, \\ \frac{dw}{dt} &= \phi [w_\infty(V) - w] / \tau_w(V). \end{aligned} \quad (3.1)$$

The activation variable w is the fraction of K^+ channels open, and provides the slow voltage-dependent negative feedback as required for excitability. The V -dependence of τ_w , m_∞ and w_∞ is shown in Figure 9A. We use the same values of model parameters as in [53]. They are summarized in the caption to figure 9 and are the same throughout the section unless noted otherwise.

This two-variable system's behaviors can be fully revealed in the phase plane. We start by finding the nullclines — the two curves defined by setting dV/dt and dw/dt individually equal to zero. These nullclines define some key features of the dynamics. A solution trajectory that crosses a nullcline does so either vertically or horizontally. The nullclines also segregate the phase plane into regions with different directions for a trajectory's vector flow. The nullclines' intersections are the steady states or fixed points of the system. Much can be concluded just by looking at the nullclines, and how they change with parameters. The V -nullcline is defined by

$$-I_{ion}(V, w) + I_{app} = 0.$$

To see what this curve looks like, let us say that $I_{app} = 0$, and look at the current $I_{ion}(V, w_0)$ versus V with w fixed. This is just the instantaneous $I - V$ relation $I_{ion}(V, w_0) = I_{inst}(V; w_0)$, depending on the level of w , and we want to know its zeros. Similar to the Hodgkin-Huxley model, this curve is N-shaped (see Fig. 9B1), and increasing w approximately moves the curve upward. Dependence of the zero-crossings with w will determine the V nullcline (Fig. 9B). For moderate w there are three zeros, and therefore three branches of the V -nullcline (corresponding to R, T and E: rest, threshold and the excited state); for low w there is only one high- V branch; and for large w only a low- V branch.

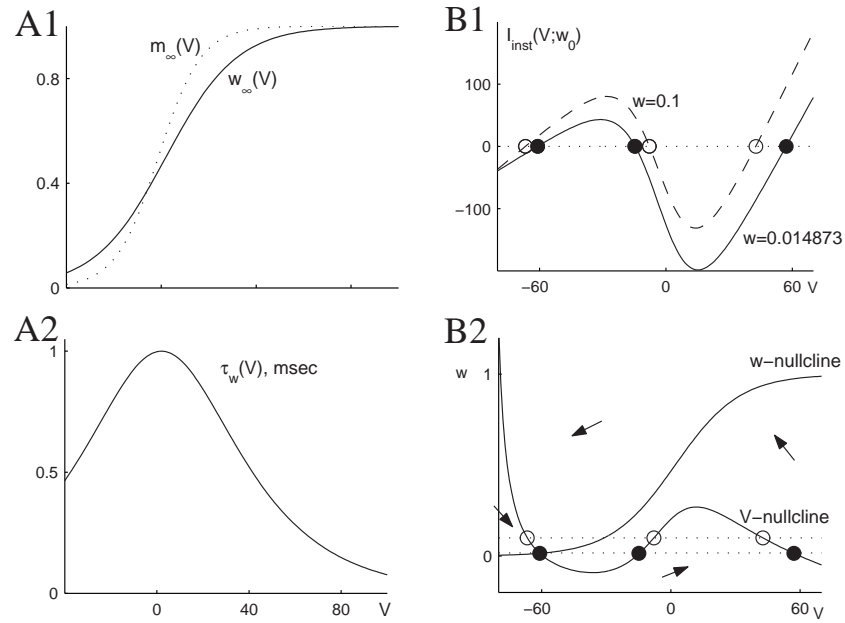


Fig. 9. *A*: Time constants and the steady state functions for the Morris-Lecar model. Upper: $m_\infty(V) = .5(1 + \tanh((V - V_1)/V_2))$ (dotted), $w_\infty(V) = .5(1 + \tanh((V - V_3)/V_4))$ (solid); lower: $\tau_w(V) = 1/\cosh((V - V_3)/(2V_4))$, where $V_1 = -1.2$, $V_2 = 18$, $V_3 = 2$, $V_4 = 30$, $\phi = .04$. Other parameters: $C = 20 \mu\text{F}/\text{cm}^2$, $\bar{g}_{Ca} = 4$, $V_{Ca} = 120$, $\bar{g}_K = 8$, $V_K = -84$, $\bar{g}_L = 2$, $V_L = -60$. *B*: Construction of the nullclines. Upper: $I_{inst}(V; w)$ for $w = 0.014873$ (at rest, solid curve) and $w = 0.1$; lower: V and w nullclines; arrows show direction of the flow in the plane. All parameter values are as in [53]. Voltages are in mV, conductances are in mS/cm^2 , currents in $\mu\text{A}/\text{cm}^2$. They are the same throughout the section unless noted otherwise.

Below the V -nullcline in the $V - w$ plane $dV/dt > 0$, i.e. V is increasing, while above the nullcline V is decreasing. The w -nullcline is simply the activation curve $w = w_\infty(V)$. Left of this curve w decreases and to the right w increases (Fig. 9B2).

The steady state solution (\bar{V}, \bar{w}) of the system is the point where the nullclines intersect. It must satisfy $I_{ss}(\bar{V}) = I_{app}$, where $I_{ss}(V)$ is the steady state $I - V$ relation of the model given by

$$I_{ss}(V) = I_{ion}(V, w_\infty(V)).$$

If I_{ss} is N-shaped, then there can be three steady states for some range of I_{app} . However, if I_{ss} is monotone (as is the case for the parameters in figure 9), then there is a unique steady state, for any I_{app} .

3.1. Excitable regime

We say that the system is in the excitable regime when it has just one stable steady state and the action potential (large regenerative excursion) is evoked following a large enough brief stimulus. Figure 10A,B shows the responses to brief I_{app} pulses of different amplitude. After a small pulse the solution returns directly back to rest (subthreshold). If the pulse is large enough, autocatalysis starts, the solution's trajectory heads rightward toward the V -nullcline. After the trajectory crosses the V -nullcline (vertically, of course) it follows upward along the nullcline's right branch. After passing above the knee it heads rapidly leftward (downstroke). The number of K^+ channels open reaches a maximum during the downstroke, as the w -nullcline is crossed. Then the trajectory crosses the V -nullcline's left branch (minimum of V) and heads downward, returning to rest (recovery).

Notice that if a superthreshold pulse initiates the action potential with different initial conditions (say, closer to the V -nullcline's middle branch), then the solution does not go as far rightward in V , resulting in an intermediate amplitude (graded) response. This contradicts the traditional view that the action potential is an all-or-none event with a fixed amplitude. This possibility of graded responsiveness in an excitable model was first observed by FitzHugh [23], in studying an idealized analytically tractable two-variable model. His model is often considered as a prototype for excitable systems in many biological and chemical contexts. But in that model, as well as in the Hodgkin-Huxley model and in the Morris-Lecar example of Fig. 10A, there is not a strict threshold. If we plot the peak V vs. the size of the pulse or initial condition V_0 , we get a continuous curve (Fig. 10C). The steepness of this curve depends on how slow is the negative feedback. If w , for example, is very slow then the flow in the phase plane is close to horizontal, V is relatively much faster than w , and it takes fine tuning of the

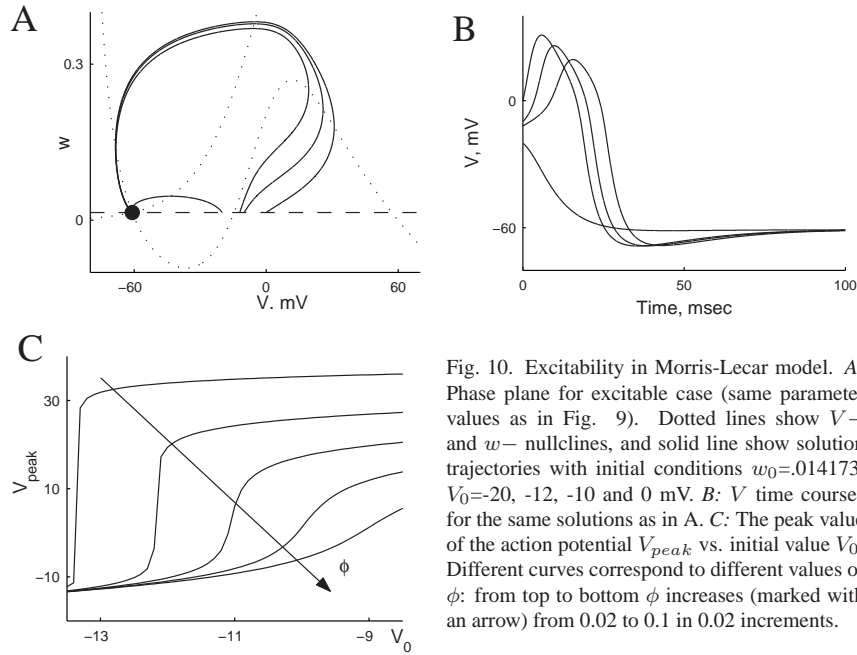


Fig. 10. Excitability in Morris-Lecar model. A: Phase plane for excitable case (same parameter values as in Fig. 9). Dotted lines show V - and w - nullclines, and solid line show solution trajectories with initial conditions $w_0=0.014173$, $V_0=-20, -12, -10$ and 0 mV. B: V time courses for the same solutions as in A. C: The peak value of the action potential V_{peak} vs. initial value V_0 . Different curves correspond to different values of ϕ : from top to bottom ϕ increases (marked with an arrow) from 0.02 to 0.1 in 0.02 increments.

initial conditions to evoke the graded responses – the curve is steep. How close to horizontal the flow is, is determined by the size of ϕ :

$$\frac{dw}{dV} = \left(\frac{dw}{dt} \right) / \left(\frac{dV}{dt} \right) = O(\phi).$$

If ϕ is very small (w slow) then the trajectory of the action potential looks like a relaxation oscillator and the plateau, upstroke and the downstroke are more pronounced, like in a cardiac action potential, or an envelope of a burst pattern. This suggests that if the experimentally observed action potentials look like all-or-none events, they may become graded if recordings are made at higher temperatures. This experiment was suggested by FitzHugh and carried out by Cole et al. [11]. It was found that if recordings in squid giant axon are made at 38°C instead of, say, 15°C then action potentials do not behave in an all-or none manner.

3.2. Post-inhibitory rebound

Many neurons can fire an action potential when released from hyperpolarization. Namely, if a step with $I_{app} < 0$ is applied for a prolonged period of time

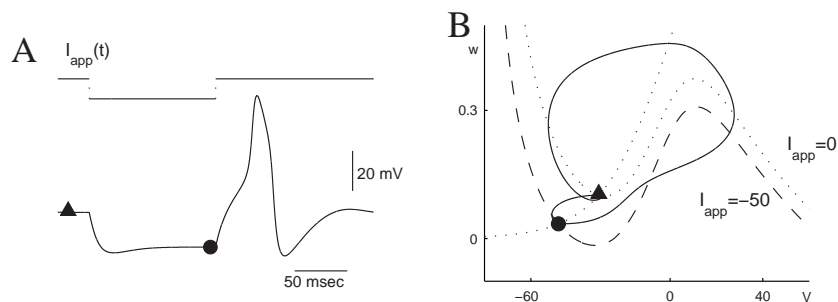


Fig. 11. Post-inhibitory rebound in Morris-Lecar model. *A*: Time courses of hyperpolarizing current and corresponding voltage. *B*: Same response trajectory as in *A* shown in the $V - w$ phase plane. Also shown are nullclines for $I_{app}=0$ $\mu\text{A}/\text{cm}^2$ (dotted) and V -nullcline for hyperpolarized current $I_{app}=-50$ $\mu\text{A}/\text{cm}^2$ (dashed). Triangle and filled circle mark steady state points for each of these cases.

and then switched off, the neuron may respond with a single spike upon the release (Fig. 11A). This phenomenon is called post-inhibitory rebound (PIR), or in the classical literature, anodal break excitation. To explain PIR, let us look at the phase-plane (Fig. 11B). Before I_{app} is turned on the resting point is on the left branch of the V -nullcline. When I_{app} comes on, it pulls the V -nullcline down. The steady state moves, accordingly, down and to the left (i.e. it becomes more hyperpolarized and with K^+ further deactivated). If the current is held long enough, then the solution settles to the new steady state. Next, when the current is released abruptly the V -nullcline snaps back up. The solution location is now below the nullcline, and if ϕ is sufficiently small, the solution will fly all the way to the right branch and then return to rest through the full action potential.

Physiologically, the rebound is possible because the K^+ channels that are usually open at rest are closed by the hyperpolarization. This makes the membrane hyperexcitable, i.e. lowers its threshold for firing. When the cell is released it takes awhile for w to activate and during this delay the autocatalytic I_{Ca} is less opposed. Anodal break excitation is also observed in the Hodgkin-Huxley model [24]. There, the hyperpolarization also causes removal of inactivation of I_{Na} (increase in h), which contributes to facilitating the rebound.

3.3. Single steady state. Onset of repetitive firing, type II

Let us ask now whether and how repetitive firing can arise in this model with I_{app} as a control parameter. As before, we will look for parameter values where the steady state is unstable, using linear stability theory. Let us say the steady state is $(\bar{V}(I_{app}), \bar{w}(I_{app}))$. Now, consider the effects of a perturbation from the

steady state: $(V(t), w(t)) = (\bar{V} + x(t), \bar{w} + y(t))$, and ask whether x and y can grow with t (unstable solution) or decay (stable solution). For the first equation:

$$\begin{aligned} C \frac{dV}{dt} &= C \frac{dx}{dt} = I_{app} - I_{ion}(\bar{V} + x, \bar{w} + y) = \\ &= I_{app} - I_{ion}(\bar{V}, \bar{w}) - \left. \frac{\partial I_{ion}}{\partial V} \right|_{(\bar{V}, \bar{w})} x - \left. \frac{\partial I_{ion}}{\partial w} \right|_{(\bar{V}, \bar{w})} y + h.o.t., \end{aligned}$$

where *h.o.t.* means higher order terms. The first 2 terms sum to zero, leaving (after neglecting h.o.t.)

$$C \frac{dx}{dt} = - \left. \frac{\partial I_{inst}}{\partial V} \right|_{(\bar{V}, \bar{w})} x - \left. \frac{\partial I_{inst}}{\partial w} \right|_{(\bar{V}, \bar{w})} y.$$

For the second equation:

$$\frac{dy}{dt} = \phi \frac{w'_{\infty}}{\tau_w} x - \frac{\phi}{\tau_w} y.$$

To summarize:

$$\frac{d}{dt} \begin{pmatrix} x \\ y \end{pmatrix} = J \begin{pmatrix} x \\ y \end{pmatrix}, \quad (3.2)$$

where J is the Jacobian matrix, evaluated at the steady state:

$$J = \begin{pmatrix} -\frac{1}{C} \left. \frac{\partial I_{inst}}{\partial V} \right|_{(\bar{V}, \bar{w})} & -\frac{1}{C} \left. \frac{\partial I_{inst}}{\partial w} \right|_{(\bar{V}, \bar{w})} \\ \phi \frac{w'_{\infty}}{\tau_w} & -\phi \frac{1}{\tau_w} \end{pmatrix} \Bigg|_{(\bar{V}, \bar{w})}.$$

Stability of the system 3.2 is determined by the eigenvalues λ_1 and λ_2 of J :

$$\det J = \lambda_1 \cdot \lambda_2,$$

$$\text{tr } J = \lambda_1 + \lambda_2.$$

For the steady state to be stable the real parts of both eigenvalues must be negative. In order for the fixed point to lose stability one of the following two things must happen:

- (1) λ_1 or λ_2 is equal to 0, i.e. $\det J = 0$;
- (2) $\text{Re}(\lambda_1) = \text{Re}(\lambda_2) = 0$, $\text{Im}(\lambda_{1,2}) \neq 0$, i.e. $\text{tr } J = 0$ — Hopf bifurcation.

Case (1) can only happen if \bar{V} is at the "knee" of $I_{ss}(V)$, because $\det J = 0 = \frac{\phi}{\tau_w} \cdot \frac{1}{C} \left[\frac{dI_{ss}}{dV} \right]$. Therefore, if I_{ss} is monotonic, the loss of stability can only happen via case (2), Hopf bifurcation.

For the parameters in figure 9 both eigenvalues are real and negative, i.e. the steady state is stable. Moreover, $I_{ss}(V)$ in this case is monotonic (as in the Hodgkin-Huxley equations) and the loss of stability can happen only through Hopf bifurcation. We have:

$$\text{tr } J = 0 = -\frac{1}{C} \frac{\partial I_{inst}}{\partial V} \Big|_{(V, \bar{w})} - \frac{\phi}{\tau_w}.$$

Instability means that this expression is positive, i.e.

$$-\frac{1}{C} \frac{\partial I_{inst}}{\partial V} > \frac{\phi}{\tau_w}. \quad (3.3)$$

This says that in order to get instability $\frac{\partial I_{inst}}{\partial V}$ must be sufficiently negative, which is equivalent to having the fixed point on the middle branch (and sufficiently away from the "knees") of the V -nullcline. Also the rate of the negative feedback $\frac{\phi}{\tau_w}$ should be slow enough. If the temperature is too high (ϕ is too large), then destabilization will not happen. Condition 3.3 can also be interpreted as the autocatalysis rate being faster than the negative feedback's rate. When this condition is met, the steady state loses stability through a Hopf bifurcation, giving rise to a periodic solution, i.e. leading to the onset of repetitive firing. This periodic solution has a non-zero frequency associated with it, which is proportional to the $Im(\lambda_{1,2})$ ([62]), i.e. the repetitive firing emerges with non-zero frequency. Figures 12B and C show the bifurcation diagram and the $f - I$ relation, respectively. Notice that this is the same type of repetitive firing onset as we have seen in the Hodgkin-Huxley equations. It is called Type II onset, following the terminology of Hodgkin [34].

Figure 12A shows snapshots of the nullcline positions at different I_{app} (the values are marked I_{excit} , I_{osc} and I_{block} in Fig. 12B), and the lower panels show the V time courses for the same values of I_{app} . For $I_{app} = I_{excit}$ the membrane is excitable (the steady state is on the left branch). Increasing I_{app} to I_{osc} shifts the V -nullcline up, and the steady state moves to the middle branch and becomes unstable. Existence of a stable periodic orbit can be shown qualitatively for ϕ small considering the direction of the flow in the phase plane: the flow is always away from the unstable point, horizontally (say to the right), then following the V -nullcline to the knee, shoots left again, etc. The cycle can also be constructed by the geometrical singular perturbation or by the Poincare-Bendixon theorem (see chapter by Terman in this volume). If I_{app} is further increased to I_{block} the steady state moves to the right branch and becomes stable again. In this state the K^+ and Ca^{2+} currents are strongly activated, but they are in a stable balance. This is nerve block — there is no firing, but the membrane is depolarized. At this point we have to remind ourselves again that this model is a description of a

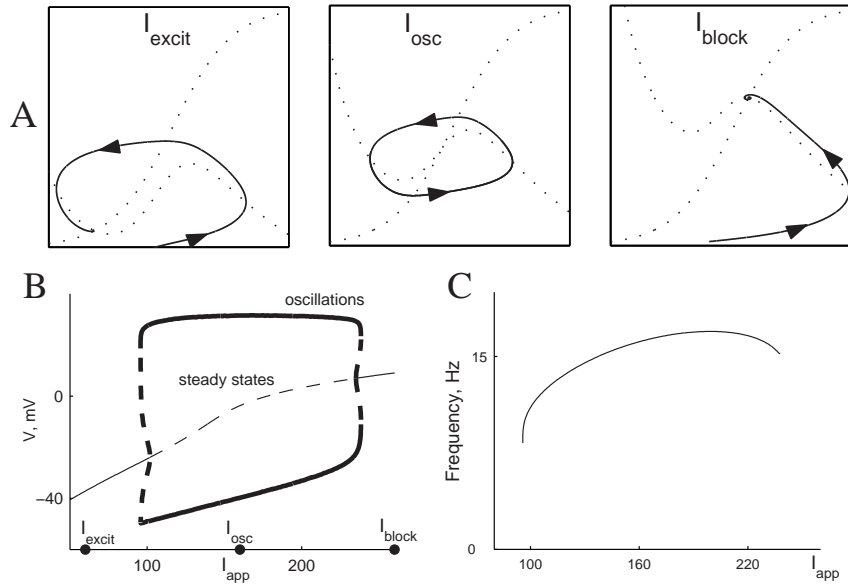


Fig. 12. Onset of repetitive firing with one steady state (Type II). *A*: Nullclines for different values of I_{app} (60, 160 and $260 \mu\text{A}/\text{cm}^2$), corresponding to excitable, oscillatory and nerve-block states of the system. *B*, *C*: Bifurcation diagram (*B*) and f-I curve (*C*). *B*: *Thin solid curves*: stable steady state, *thin dashed curves*: unstable steady state, *thick solid curves*: maximum and minimum V of the stable limit cycle, *thick dashed curves*: maximum and minimum V of the unstable limit cycle. Parameter values are the same as in figure 9.

point neuron. It does not address what is happening in the axon. In principle, the axon may be generating action potentials that we do not see in this description.

Finally, we notice in figure 12B that, as in the Hodgkin-Huxley model (see section 2.4.3) there is a range of bistability, and the solution in that range can be brought into the domain of attraction of either the fixed point or the limit cycle by brief perturbations.

3.4. Three steady states

The cases of Morris-Lecar model dynamics that we have so far considered are reminiscent of the Hodgkin-Huxley dynamics in that there is always a unique fixed point. In other parameter regimes $I_{ss}(V)$ may not be monotonic. For example, increasing \bar{V}_K to higher values [50], corresponding experimentally to increasing the extracellular K^+ concentration, can cause $I_{ss}(V)$ to become N-shaped. This means that for some values of I_{app} there are three steady states and

the curve of steady states vs. I_{app} is S-shaped (Figs. 13-15). We also choose parameters in such a way that only the lower steady state is on the left branch of the V -nullcline, while both middle and upper steady states are on the middle branch (Figs. 13-15). The number and location of steady states do not depend on temperature (i.e. on ϕ). But the stability and the onset of repetitive firing, as we have seen above, do depend on ϕ . Therefore, we will further study the dynamics at different values of ϕ .

3.4.1. Large ϕ . Bistability of steady states

We have computed above in equation 3.3 the condition for destabilization of a steady state through Hopf bifurcation. It shows that the negative feedback from w has to be sufficiently slow compared to V for the bifurcation to happen. For large ϕ this condition is not satisfied. Moreover, for large ϕ w is so fast that it can be considered as instantaneous $w = w_\infty(V)$. Then the model is reduced to one dynamic variable V and the stability of the steady states is simply determined by the sign of $\frac{dI_{ss}}{dV}$, i.e. the middle steady state is unstable and the upper and lower ones are stable. Figure 13A shows the $V - w$ phase plane with steady states and nullclines for increased ϕ . There is again a range of bistability, but in this case it is bistability between two steady states — with higher and lower voltage. The voltage can be switched from one constant level to the other by brief pulses (Fig. 13B). This type of behavior is sometimes called “plateau behavior” and it has been used in models describing vertebrate motoneurons [4].

3.4.2. Small ϕ . Onset of repetitive firing, Type I

If ϕ is very small (Fig. 14A1), then according to the instability condition 3.3 both middle and upper steady states can be unstable for a range of I_{app} . (Notice that when there are three fixed points in the system they are not always “stable-unstable-stable”!) The middle fixed point is a saddle. One of the branches of its unstable (“outgoing”) manifold goes directly to the stable steady state, and the other branch goes around the unstable spiral and also comes back to the stable point. These two unstable manifold branches are heteroclinic orbits — connecting two singular points. They effectively form (topologically) a circle that has two fixed points on it (Fig. 14A2, left panel). As I_{app} is increased, the V -nullcline moves up and the stable fixed point and the saddle must coalesce and disappear. Figure 14A2, middle and right panels, show this bifurcation schematically. As the two points coalesce and then disappear the orbits connecting them form a single limit cycle. For I_{app} exactly at the critical value I_1 the limit cycle has infinite period, i.e. the closed trajectory is a homoclinic orbit. Such an orbit is called (by some dynamicists) a saddle-node on an invariant circle (SNIC). For I_{app} just above the critical value the frequency is proportional to $\sqrt{I_{app} - I_1}$ (see [62]), i.e. the repetitive firing emerges with zero initial frequency and high

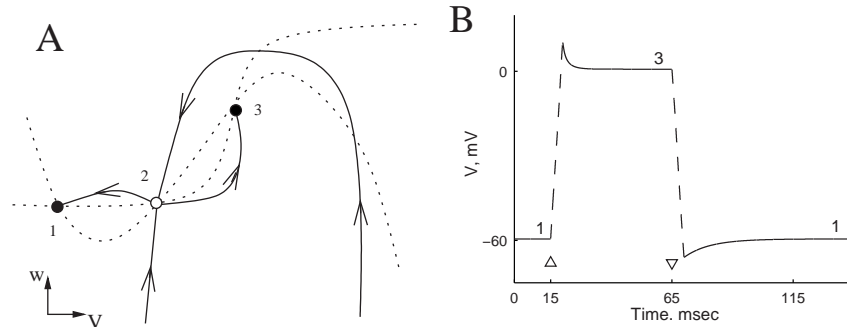


Fig. 13. Large ϕ case. A: Schematic of $V - w$ phase plane with steady states (filled circles – stable steady states, open circle – unstable), nullclines (dotted curves), and trajectories going in and out the saddle point (solid curves). The curves are slightly modified from the actual computed ones for easier viewing; in particular, the trajectories emanating from the saddle would not have extrema away from nullclines. B: Switching the solution from one stable steady state (marked 1 in A) to the other (marked 3 in A) and back with brief current pulses. Parameters are the same as in Fig. 9, except $V_3 = 12$ mV, $V_4 = 17$ mV, $\phi = 1$. Depolarizing pulse of strength $250 \mu\text{A}/\text{cm}^2$ is applied at $t = 15$ msec, hyperpolarizing pulse of strength $-250 \mu\text{A}/\text{cm}^2$ is applied at $t = 65$ msec; duration of each pulse 5 msec.

amplitude. Figure 14B shows an example of the V time-course with I_{app} not far above the critical value, and the period of spiking is very large.

The bifurcation diagram for this case is shown in Fig. 14C and the $f - I$ curve in Fig. 14D. As I_{app} increases beyond the saddle-node bifurcation the frequency of the oscillation increases while the amplitude decreases. The oscillatory solutions terminate via subcritical Hopf bifurcation, generating a small range of bistability.

Emergence of oscillatory behavior with arbitrary low frequencies has been reported in other models as well as in experiments (for example [12, 27, 31, 59]). Sometimes this zero-frequency onset has been attributed to the presence of an inactivating potassium A-type current ([12], although as we see here such an I_K is not required [58]).

3.4.3. Intermediate ϕ . Bistability of rest state and a depolarized oscillation

At intermediate values of ϕ both middle and upper steady states can be unstable, but the upper steady state is surrounded by a stable periodic orbit (Fig. 15A). In this case there is bistability between the low-voltage stationary point and depolarized repetitive firing. As before, brief I_{app} pulses can be used to switch between the states (Fig. 15B). The saddle's stable manifold serves as the separatrix between the domains of attraction of the two states. The model also predicts

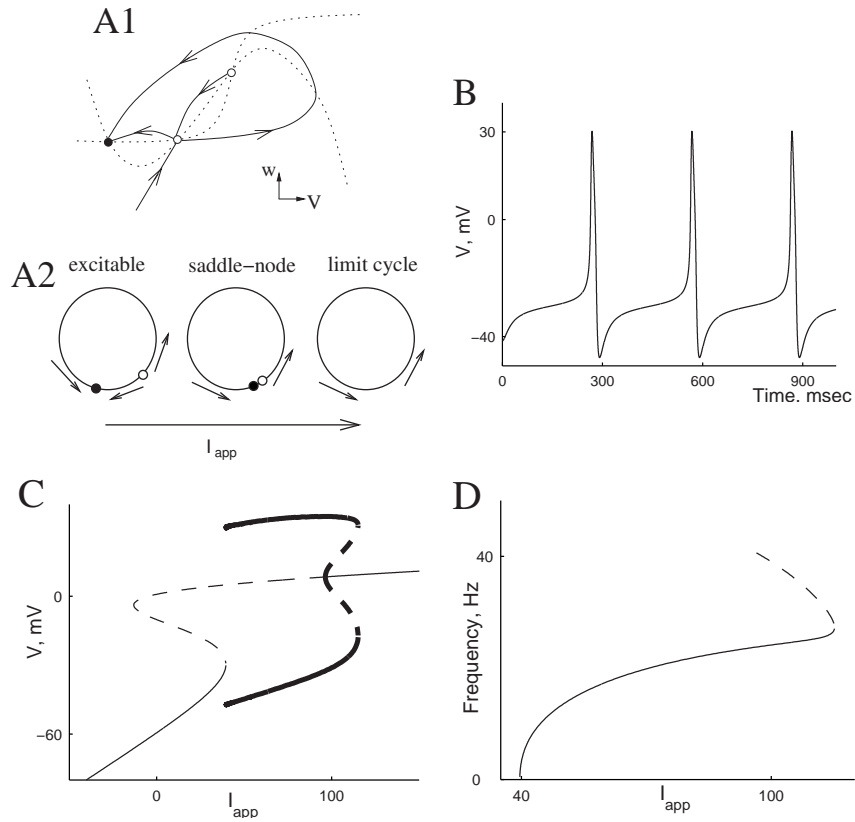


Fig. 14. Small ϕ case. Parameters are the same as in Fig. 13, except $\phi = .06666667$. A: Schematics of phase plane. A1: Schematic of phase plane for $I_{app} = 0 \mu A/cm^2$. Notations are the same as in Fig. 13A. The curves are slightly modified from the actual computed ones for easier viewing; in particular, actual trajectories would not have extrema away from nullclines. A2: Schematic of change in phase plane with change of I_{app} (see text). B: Time course of voltage for $I_{app} = 40 \mu A/cm^2$. C: Bifurcation diagram. Notation the same as in Fig. 7. D: $f - I$ curve. Dashed portion corresponds to unstable periodic orbit.

that if a perturbation from rest is too large, then the system will exhibit one spike and come back to rest, not to the cycle. This happens, mathematically, because the perturbation causes the solution to cross the separatrix twice (see Fig. 15A), and, biophysically, because too much I_K gets recruited. This phenomenon in the model has yet to be demonstrated experimentally, to our knowledge.

To see how this phase plane portrait arises, let us look at the bifurcation diagram in Fig. 15C. The lower steady state is stable for all I_{app} and the middle one, a saddle, is always unstable. When I_{app} is very high a block occurs. When I_{app} is decreased from large values, the high- V steady state loses stability through a subcritical Hopf bifurcation. The emergent branch of (unstable) periodic orbits bends rightward from the Hopf point, but then turns around, stabilizing at the knee. So for some range of I_{app} there are three steady states and two periodic states. An example from this range of I_{app} is shown in figure 15A. As I_{app} is decreased further the stable periodic orbit's minimum V drops enough to contact the saddle, terminating the periodic branch. At this critical value of $I_{app} = I_1$ when the limit circle collides with the saddle, the unstable manifold of the saddle leaves the fixed point along the cycle and then returns back along the cycle as the stable manifold. This homoclinic loop is called a "saddle loop homoclinic orbit". The firing rate in this case also emerges from zero, but it increases as $1/|\ln(I_{app} - I_1)|$ (Fig. 15D, see also [62]).

This example in which a stable rest state coexists with a depolarized limit cycle provides the basis for square wave bursting (see section 4).

3.5. Similar phenomena in the Hodgkin-Huxley model

In section 2 we saw that in the Hodgkin-Huxley model repetitive firing emerges through a Hopf bifurcation with small amplitude and non-zero frequency. In fact, the Hodgkin-Huxley model can be tuned into parameter regimes that yield most of the dynamic behaviors that we described for the Morris-Lecar model [50]. For increased \bar{V}_K $I_{ss}(V)$ becomes N-shaped, because K^+ now has a reversal potential that is not below resting V . If we also vary the temperature, the model will be tuned into plateauing behavior (coexistence of two steady states) or the type of behavior that we described for intermediate ϕ in Morris-Lecar model (resting state and a depolarized stable cycle).

3.6. Summary: onset of repetitive firing, Types I and II

Here we summarize the characteristic properties of two generic types of transition from the excitable to oscillatory mode in neuronal models.

Type II: (1) I_{ss} monotonic; (2) subthreshold oscillations; (3) excitability without distinct threshold; (4) excitability with finite latency.

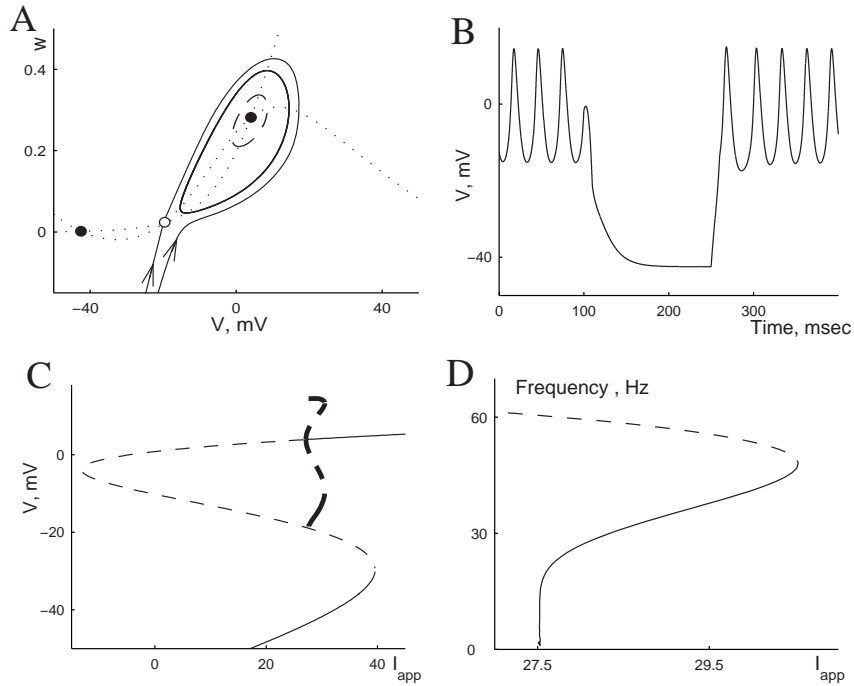


Fig. 15. Intermediate ϕ case. Parameters are the same as in Fig. 13, except $\phi = .25$. A: $V - w$ phase plane for $I_{app} = 30 \mu A/cm^2$. Dotted curves are nullclines, solid closed curve is the stable periodic orbit, dashed closed curve is the unstable periodic orbit. There are 2 stable steady states (filled circles) and one unstable steady state (open circle). Solid curves with arrows mark the trajectories going into the saddle point. B: Switching of V from the stable periodic orbit to lower steady state and back for $I_{app} = 30 \mu A/cm^2$. Hyperpolarizing pulse of amplitude $-100 \mu A/cm^2$ and duration 1 msec arrives at $t = 100$ msec and depolarizing pulse of amplitude $100 \mu A/cm^2$ and duration 5 msec arrives at $t = 250$ msec. C: Bifurcation diagram for $\phi = 0.25$. Thin solid curves: stable steady state, thin dashed curves: unstable steady state, thick solid curves: maximum and minimum V of the stable limit cycle, thick dashed curves: maximum and minimum V of the unstable limit cycle. D: f-I curve. Dashed portion corresponds to unstable periodic orbit.

Type I: (1) I_{ss} N-shaped; (2) no subthreshold oscillations; (3) all-or-none excitability with strict threshold; (4) infinite latencies.

The two cases also have different ($f - I$) relations. However, if there is noise in the system, the $f - I$ curves for both types will become qualitatively similar. The discontinuity of Type II will disappear with noise since the probability of firing becomes non-zero where it was zero before. Type I's $f - I$ curve will also inherit a smooth foot rather than the infinite slope at zero frequency due to the noise-free case's square root rise (see, for example [31]).

4. Bursting, cellular level

Bursting is an oscillation mode with relatively slow rhythmic alternations between an active phase of rapid spiking and a phase of quiescence. A classical case, and well studied (both experimentally and theoretically), is the parabolic bursting R_{15} neuron of the *Aplysisa*'s abdominal ganglion [2, 63]. Since its early discovery bursting has been found as a primary mode of behavior in many nerve and endocrine cells. Many of the experimentally found examples have been successfully modeled — sometimes with very good agreement between the data and the model. A collection of experimental examples and models was presented by Rinzel and Wang [70], including bursting in pancreatic β -cells, dopaminergic neurons of the mammalian midbrain, thalamic relay cells, inferior olive cells, and neocortical pyramidal neurons. Several classification schemes of different types of bursting, based on the bifurcation structure of the corresponding mathematical models, have been developed e.g. by Rinzel [51], Bertram et al. [3], de Vries [68], Izhikevich [36], Golubitsky et al. [28]. These classifications characterize the bursting behaviors by describing the topologies of the sequence of invariant sets that the solutions visit (steady states, periodic orbits, etc.) and the ways in which the solutions move between the sets (topological structure of the bursting). They also describe phenomenological properties of different types of bursting, for example, the shape and the amplitude of the spikes, evolution of spiking frequency during the active phase, presence or absence of bistability, etc. These phenomenological properties may be identified experimentally, and used for classification of biological bursters.

Biophysically the rhythmicity in bursts is generated by an autocatalytic depolarization process and slower negative feedback. In some burst mechanisms there is a distinct slow autocatalytic process (in addition to fast autocatalysis of spike generation) with even slower negative feedback, as in the case of R_{15} . In this case the spike generation can be disabled and an underlying slow rhythm, on which spike bursts ride, may persist. In other examples the fast autocatalysis of spike generation is adequate to guarantee an active phase and then a single slow

(burst time scale) negative feedback process will drive the alternation back and forth over a hysteresis loop (as suggested by Figs. 7 and 15).

For more complete presentations and mathematical details of bursting types the readers are referred to the original papers. In this section we review geometrical methods for fast-slow analysis of bursting and some examples of the different oscillation types. We describe mathematical features of some illustrative examples in the classifications and phenomenological features that can help to identify them in the experiments. For some examples we also describe ionic conductance mechanisms that are sufficient to produce these oscillations and examples of experimental systems where this bursting type has been observed.

4.1. Geometrical analysis and fast-slow dissection of bursting dynamics

The general framework described here was first used for analysis of bursting in [50,51], and then extended, for example, in [3,70]. We consider a point neuron model and separate all dynamic variables into two subgroups: “fast” (denoted as X) and “slow” (denoted as Y). In the context of bursting analysis a variable is considered fast if it changes significantly during an action potential, and a variable is considered slow if it only changes significantly on the time scale of burst duration, not during single spikes. In this formulation both V and w of the above Morris-Lecar examples fall into the “fast” category — they both participate in the spike generation mechanism, even though w may be noticeably slower than V . The model equations can now be written as:

$$\begin{aligned}\dot{X} &= F(X, Y), \\ \dot{Y} &= \epsilon G(X, Y).\end{aligned}$$

In the second group of equations ϵ is a small parameter indicating the slower time scale. The slow variables can represent the gating variables with very slow kinetics (e.g., inactivation of a low threshold I_{Ca} or slow V -gated activation of some I_K), ionic concentrations (for example, intracellular concentration of Ca^{2+}), second messenger variables, etc. We focus on cases in which the dynamics of Y depends on X , i.e. on activity-dependent feedback from the fast subsystem. In special cases where it does not, i.e., $G(X, Y) = G(Y)$, the fast subsystem is driven non-autonomously by the slow subsystem; the slow burst rhythm cannot be reset by brief perturbations to the fast subsystem variables.

The analysis of the system can be conducted in two steps.

Step 1. First we think of the slow variables as parameters and describe the spike-generating fast subsystem for X as a function of Y . This description involves finding steady states, oscillatory orbits and their periods, and transitions between all these solutions (bifurcations) as a function of Y :

$$0 = F(X_{ss}, Y) \implies X_{ss} = X_{ss}(Y)$$

or

$$\dot{X}_{osc} = F(X_{osc}, Y) \implies X_{osc}(t) = X_{osc}(t + T), T = T(Y).$$

If Y is one-dimensional (there is only one slow variable) then the results can be summarized in a bifurcation diagram of the same type as we have seen above, with Y as the bifurcation parameter. When Y is multi-dimensional it simply adds dimensions to the bifurcation diagram and it may become harder to visualize.

Step 2. To describe the full system we overlay the slow dynamics on the fast system behavior. Y evolves slowly in time according to its equations, while X is tracking its stable states. Therefore, we must understand the direction of change of Y at each part of the bifurcation diagram for X .

When the full burst dynamics is projected to the (Y, V) plane, it coincides with portions of the bifurcation diagram. The results of this analysis allow one to make phenomenological descriptions of the bursting behavior and predict effects of parameter changes on behavior.

4.2. Examples of bursting behavior

4.2.1. Square wave bursting

Square wave bursting (see Fig. 16) is characterized minimally by a single slow variable (i.e., Y is a scalar) and the fast subsystem structure is qualitatively as described in section 3.4.3 above. To recall, in the fast subsystem there is an S-shaped curve of steady states. The lower steady state is stable and corresponds to the silent phase of the bursting solution (Fig. 16B). The upper steady state is surrounded by an oscillatory state which corresponds to the active phase of firing. The oscillatory state terminates when it contacts the middle branch in a saddle-loop homoclinic bifurcation. At the intermediate range of the parameter values there is bistability between the lower steady state and the "upper" periodic orbit (Fig. 16B). Next, the kinetics of the slow parameter Y has to be such that Y decreases when the fast subsystem is at the low steady state and increases when the fast subsystem oscillates around the upper steady state. This dynamics of Y allows fast switching between coexistent stable states, generating bursting, as shown in Fig. 16A. The active phase begins at the saddle-node bifurcation and terminates at the saddle-loop. (Note, it is not essential in Fig. 15 that the Hopf bifurcation on the high- V branch be subcritical.)

Phenomenologically, square wave bursting is characterized by abrupt periodic switching between a silent phase and a state of depolarized repetitive firing. Moreover, the spikes typically ride on a plateau (i.e., do not undershoot), spike frequency decreases towards the end of the active phase (due to proximity to a homoclinic), and the burst rhythm's phase can be reset by brief pulses of I_{app} (due to bistability).

The seminal work of Hodgkin-Huxley -like modeling of square wave bursting [7] was for the electrical activity of pancreatic β -cells, leading to the subsequent mathematical treatment and characterization of fast-slow analysis ([50]).

In a number of minimal biophysical models for square wave bursting, spiking is due to high-threshold Ca^{2+} and delayed-rectifier K^+ currents; bursting is due to either a calcium-activated potassium current [7, 50] or due to slow inactivation of the Ca^{2+} current by feedback from voltage or from Ca^{2+} concentration itself [14]. The I_{K-Ca} bursting mechanism, for example, depends on the slow dynamics of Ca^{2+} -handling in the cell. It works in the following way. During the active phase each spike slightly increases Ca^{2+} concentration inside the cell, which in turn activates a bit of the I_{K-Ca} current. When the potassium current is large enough, it brings the voltage down, terminating the active phase. During the silent phase Ca^{2+} influx is minimal and Ca^{2+} concentration slowly decreases turning off I_{K-Ca} until spiking can resume. In these models of square wave bursting intracellular Ca^{2+} concentration Ca satisfies

$$\dot{Ca} = f [-\alpha I_{Ca} - k \cdot Ca],$$

where f is the buffering constant $f = \frac{[Ca_{free}^{2+}]}{[Ca_{TOT}^{2+}]}$, and the Ca^{2+} concentration is increased by the inward (i.e. negative) membrane calcium current I_{Ca} and calcium is removed from the cytoplasm with rate k . The slow time scale is due to the fact that f is small (say, 0.01 or so); most of the Ca^{2+} that enters the cell is rapidly buffered by reversible binding to sites on various molecules inside the cell. As the removal rate k is increased parametrically the behavior changes from a low- V steady state, to bursting, to continuous spiking.

Multiple biophysical mechanisms have also been modelled to account for square bursting in brain stem neurons that are involved in neural circuits that drive respiration (see [5] and Fig. 1C,D in this chapter).

4.2.2. Parabolic bursting

Parabolic bursting is generated without bistability in the fast subsystem and it requires at least two-variables in the slow subsystem. Steady states of the fast subsystem are now represented as an S-shaped surface over the two-dimensional plane of slow variables. Oscillatory solutions, similarly, are also represented as surfaces. They terminate as they touch the steady state surface at the (say, low- V) knee in a SNIC bifurcation. If the fast subsystem bifurcation surface is projected down to the slow-variable plane, the plane is divided into two non-overlapping regions: one with the resting steady state and the other with the repetitive firing for the fast subsystem. The dynamics of the slow variables is designed in such a way that there is an oscillation in this slow-variable plane that visits both regions

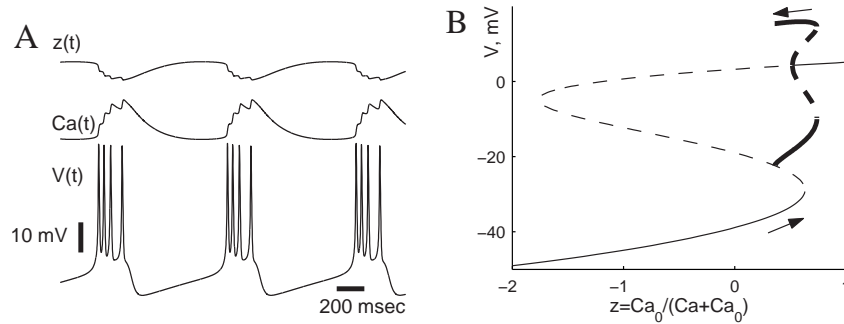


Fig. 16. Square wave burster. Equations and parameters are the same as in Fig. 15 with $I_{app} = 45 \mu\text{A}/\text{cm}^2$ and an additional Ca^{2+} -dependent K^+ current $I_{K-Ca} = g_{K-Ca}(1-z)(V - V_K)$, where $g_{K-Ca} = .25 \text{ mS}/\text{cm}^2$, gating variable $z = Ca_0 / (Ca + Ca_0)$, Ca^{2+} concentration is governed by $\dot{Ca} = \epsilon(-\mu \cdot g_{Ca} m_\infty(V)(V - V_{Ca}) - Ca)$, $Ca_0 = 10$, $\epsilon = 0.005$, $\mu = 0.2$. *A*: Bursting time course. Ca^{2+} is playing the role of a slow variable, accumulating during the burst and slowly decaying during the silent phase. This is entered into the original equation through the I_{K-Ca} term. The quantity that we use as a bifurcation parameter is a function of Ca : $z = Ca_0 / (Ca + Ca_0)$ (top trace). *B*: Bifurcation diagram with z as a parameter (compare to Fig 15C). Arrows show direction of change of z during the firing and during the silent phase.

(Fig. 17A), creating bursting. An active phase begins and ends with the system's trajectory crossing a SNIC bifurcation.

The monostability of the fast subsystem allows parabolic bursting to have smooth transitions between silent and active phases and to ride on a smooth sub-threshold wave (Fig. 17B). It also precludes resetting of this bursting by brief perturbations. Because the bursting trajectory passes through the homoclinic bifurcation, the spike frequency at the beginning and at the end of the active phase is reduced, hence the time course of the spike frequency has a parabolic shape, giving this bursting type its name.

Parabolic bursting was observed, probably first, in the *Aplysia* R15 neuron [1], and described with minimal biophysical models [46, 51, 56], and with various more detailed models (e.g., [6]). Experimentally, the sodium spikes during a burst can be blocked to reveal an underlying slow periodic wave generated mainly by Ca^{2+} current. In the model [56] of the slow activation of this Ca^{2+} current and its even slower inactivation by internal Ca^{2+} concentration provide the two variables for the slow subsystem.

4.2.3. Elliptic bursting

In the case of elliptic bursting the fast subsystem has bistability due to a sub-critical Hopf bifurcation (as, for example, in the Hodgkin-Huxley model, Fig. 7),

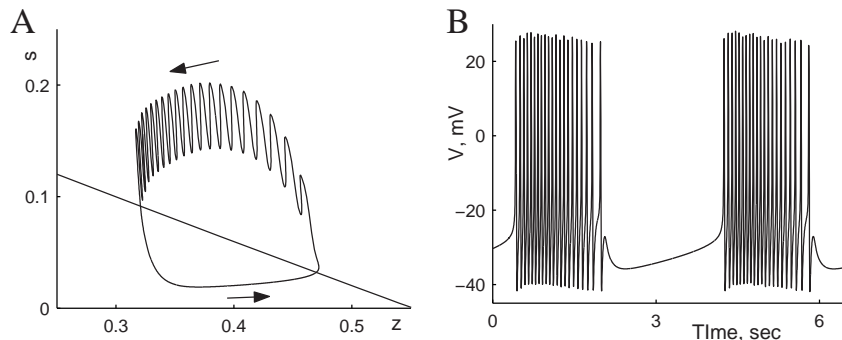


Fig. 17. Parabolic burster. Equations and parameters are the same as in Fig. 14 with $I_{app} = 65 \mu\text{A}/\text{cm}^2$ and the same Ca^{2+} -dependent K^+ current $I_{K-\text{Ca}}$ as in Fig. 16. One slow variable will be $z = \text{Ca}_0/(\text{Ca} + \text{Ca}_0)$ as in Fig. 16 above, and the second slow variable will be gating variable s of another, slow, Ca^{2+} current $I_{\text{Ca},s} = g_{\text{Ca},s}(V - V_{\text{Ca}})$. Parameter values: $g_{K-\text{Ca}} = .1 \text{ mS}/\text{cm}^2$, $\text{Ca}_0 = 1$, $\epsilon = 0.0005$, $\mu = 0.25$, $g_{\text{Ca},s} = 1 \text{ mS}/\text{cm}^2$, as in [53]. *A*: Projection of the bursting trajectory to the slow-variable plane. Direction of movement is indicated with arrows. Below the straight-looking curve low-voltage steady state is the only fast-subsystem attractor (silent phase) and above this curve there is an oscillation of the fast variables (spiking). *B*: Time course of voltage.

and the curve of steady states can be monotonic. As for square wave bursting, the mechanism requires one slow variable and Y alternates back and forth through the region of bistability, allowing the switching between the steady state and the oscillatory solution (Fig. 18A, B). Unlike the above types of bursting, though, the elliptic burster exhibits subthreshold oscillations in the silent phase, and the oscillations grow as the steady state becomes unstable through Hopf bifurcation (Fig. 18C). The active phase starts near the subcritical Hopf (just before or after, depending on whether or not some noise is present) and terminates at the saddle-node bifurcation of periodic orbits.

In elliptic bursting the envelope of the oscillatory events is modulated at very low frequency (creating an “elliptical” shape), small amplitude just before and after the large amplitude of the burst spikes. The frequency of the “silent” phase’s subthreshold oscillations is comparable to that of the Hopf bifurcation, and may or not be similar to the firing rate during bursts. The burst rhythm’s phase can be reset by brief pulses. Elliptic bursting has been described in several computational models [16, 58, 69].

4.2.4. Other types of bursting

There are many other types of bursting that have been observed experimentally, and/or constructed theoretically based on the same principles that we have just illustrated. Their classification based on the topology of the underlying structure,

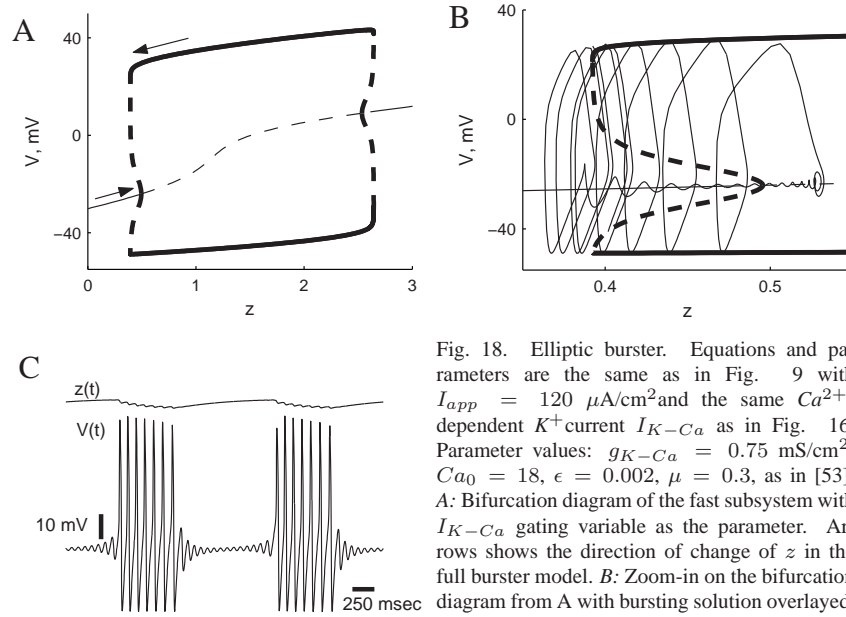


Fig. 18. Elliptic burster. Equations and parameters are the same as in Fig. 9 with $I_{app} = 120 \mu\text{A}/\text{cm}^2$ and the same Ca^{2+} -dependent K^+ current $I_{K-\text{Ca}}$ as in Fig. 16. Parameter values: $g_{K-\text{Ca}} = 0.75 \text{ mS}/\text{cm}^2$, $\text{Ca}_0 = 18$, $\epsilon = 0.002$, $\mu = 0.3$, as in [53]. *A*: Bifurcation diagram of the fast subsystem with $I_{K-\text{Ca}}$ gating variable as the parameter. Arrows shows the direction of change of z in the full burster model. *B*: Zoom-in on the bifurcation diagram from *A* with bursting solution overlaid. *C*: Time course of V and the slow variable z .

rather than on phenomenological description, is not only more accurate, but its predictions are more reliable. The reason for this is that sometimes visually similar bursting patterns can have different ionic and other biophysical mechanisms associated with them. Conversely, sometimes bursting patterns that phenomenologically appear quite different are actually found to belong to the same class, with variations in some parameters. For example, Type Ib and Type IV bursting of Bertram et al. [3] appear to be different from square wave bursting at least in that they have undershooting spikes. However, both of them were revealed to be relatively minor modifications of the square wave bursting.

As in the rest of this chapter, we have focused on bursting mechanisms in isopotential, point neuron models. We would like to note, however, that bursting can also arise due to interactions between different parts of cells, or, in a model, between different compartments (e.g. in pyramidal neocortex cells [13, 45, 66]). In a recent example, ghostbursting [17] of pyramidal cells in the electrosensory organ of weakly electric fish was studied both experimentally and theoretically. It was shown that this type of bursting depends on dendritic properties.

Bursting can also be created via the interaction of many non-bursting cells in a network, as we describe in the next section, rather than by intrinsic cellular

mechanisms.

5. Bursting, network generated. Episodic rhythms in the developing spinal cord

In this section we present an example of a model which is similar in form to the models described above, and which can be studied with similar methods, but which represents activity of a large network of cells, rather than a single cell.

5.1. Experimental background

Many developing neuronal systems exhibit spontaneous activity that is crucial for development. For example, in embryonic rat retina the ganglion cells are spontaneously active [25]. Moreover, the neighboring cells fire synchronous bursts while the activities of cells that are far apart (for example, in different eyes) are uncorrelated. This difference in the degree of synchrony in the spontaneous activity is thought to underlie the formation of ocular dominance regions in the lateral geniculate nucleus, the target of retinal output. In embryonic chick spinal cord the cells exhibit population bursts of activity (called episodes) with episode durations on the order of tens of seconds, and long inter-episode intervals of 2-10 minutes ([42, 43]). Figure 19 shows an example of such a recording. The recording is made from a bundle of fibers that carry the (motoneuron) output of a segment of the spinal cord. The signal represents the combined activity of a large population of cells. During each episode single cells fire at 20-30 Hz, while the frequency of “population cycles” within an episode is about 0.5 Hz. This pattern of population activity is very robust, and it is generated spontaneously. This means that an isolated section of the spinal cord will produce this activity without any external inputs.

Before introducing the model we identify from the experimental data the key network properties that are essential for such rhythmogenesis. First of all, cells that are intrinsic bursters have not been found in this network. The percentage of cells that are pacemakers (fire periodically in isolation) is estimated to be less than 5%. Therefore, the rhythm is thought not to be a direct consequence of the cells’ intrinsic properties alone. Second, if excitatory (glutamatergic) connections are blocked, the rhythm persists [8], i.e. the mechanism of rhythm generation is not dependent on the glutamatergic synapses. However, at this stage in development GABA-A synapses (usually associated with inhibition) can cause depolarization, i.e. be “excitatory” in effect. This is due to the fact that the Cl^- reversal potential is about -30, -40 mV, i.e. close to or even above the threshold for firing. This phenomenon is observed in many developing systems, for example in retina [25].

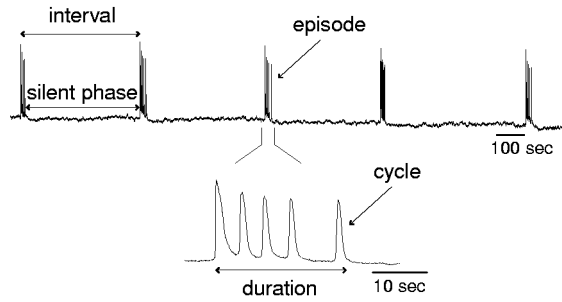


Fig. 19. Population activity of network of cells in a segment of an embryonic chick spinal cord (adapted from [65]).

Experiments also show that the size of the evoked synaptic potentials in the network is transiently reduced after an episode of spontaneous activity [21]. Shorter episodes cause less reduction of evoked synaptic potentials. These experimental observations led to the hypothesis that the episodes of activity can be terminated by the accumulated reduction in the synaptic efficacy and initiated after the synaptic recovery [43]. The primary goal of the modeling is to test this hypothesis.

5.2. Firing rate model

This model describes only the average firing rate of the population, rather than the instantaneous membrane potential and spikes of the individual neurons. It assumes a purely excitatory recurrent network in which synaptic coupling is susceptible to both short- and long-term, very slow, activity-dependent depression. The model is described by only three coupled nonlinear differential equations. Therefore, the analysis can be done graphically, step by step, which facilitates an intuitive understanding of the network dynamics.

5.2.1. Basic recurrent network

A basic model of the excitatory recurrent network can be written as:

$$\tau_a \dot{a} = a_\infty(\text{input}) - a.$$

Here a is the population activity or mean firing rate, and a_∞ is the input-output relation of a neuron, taken to be an increasing sigmoidal function. τ_a is an effective time constant, reflecting integration time within a cell and recruitment time in the network. Because the network is recurrent the input is proportional to the activity of the network itself:

$$\tau_a \dot{a} = a_\infty(n \cdot a) - a.$$

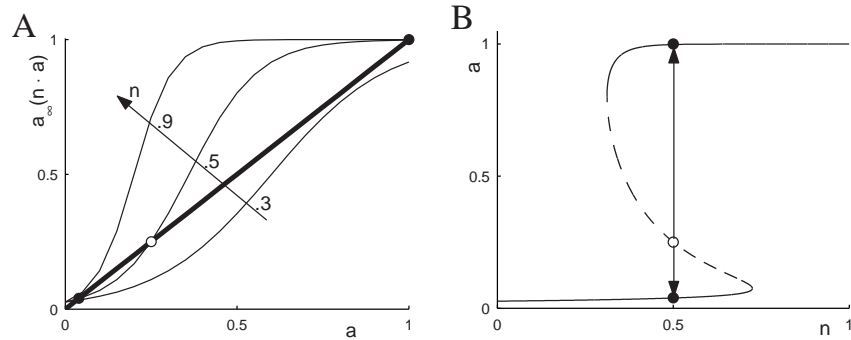


Fig. 20. Basic recurrent network. *A*: Population input-output function $a_\infty(n \cdot a)$ plotted vs. a for different values of n (thin). For each of these curves points of its intersection with line $y = a$ (thick) determine the steady states of the population at a particular level of n . These points are replotted in the $n - a$ plane in *B*. This is the curve of the steady states and its middle branch is unstable (dashed, and open circles).

The coefficient of proportionality n represents the efficacy of coupling. The steady state activity of this network depends on n (see Fig. 20A). For low n there is only one stable low activity steady state; for n high there is only one stable state, of high activity. And for intermediate values of n there are three steady states, the middle of which is unstable and the lower and upper ones are stable.

Next, we allow the effective n to vary dynamically. Based on the assumption that there is synaptic depression the synaptic efficacy n should not only vary with time, but be activity dependent. Figure 20B gives a hint of how the full model will work. When a is low, the synapses are recovering, i.e. n is increasing and the steady state moves along the lower branch of the curve to the right. When the solution reaches the knee of the curve, the steady state switches to the upper branch, which corresponds to high a . The population activity is now high which leads to depression of synapses (n decreases), until the solution crashes back to the lower branch.

5.2.2. Full model

The full model is described by three differential equations with both “fast” and “slow” depression [65]. Slow depression governs the initiation and termination of the episodes, while fast depression allows cycling within an episode. The equations of the model are:

$$\begin{aligned} \tau_a \dot{a} &= a_\infty(s \cdot d \cdot a) - a, \\ \tau_d \dot{d} &= d_\infty(a) - d, \end{aligned}$$

$$\tau_s \dot{s} = s_\infty(a) - s.$$

The product $s \cdot d$ gives the available synaptic efficacy or fraction of synapses not affected by depression. It has one component (d) that changes on a faster time scale, and the other component s that is very slow. The functions d_∞ and s_∞ are depression (turn-off) functions or efficacy recovery functions; they are sigmoidally decreasing with a from 1 to 0. The parameters of the model can be found in [65].

To understand the behavior of the model we first treat the slow variable s as a parameter and study the $a - d$ dynamics. We would like to design the two-dimensional $a - d$ system in such a way that at low values of the parameter s the solution rests at a low-activity steady state (inter-episode interval), and for high s the solution oscillates (episode). Moreover, there needs to be an overlap (bistability) between oscillation and the steady state so that s can provide transition from one to the other.

For a range of values of s there is a limit cycle oscillation in the $a - d$ plane. It originates because the recurrent excitation a provides the autocatalysis and d provides a delayed negative feedback. As activity grows, synapses start to depress, and eventually the depression reduces the activity. As a is reduced, d starts to recover and allows a to grow again, repeating the cycle (see Fig. 21A). If s is small, then there is only one stable steady state in the $a - d$ plane at low values of a . However, it is possible to choose parameters in such a way that there are three steady states, only the one with lowest a is stable, and there is a small stable limit cycle around the upper one (Fig. 21B). Figure 22A shows the bifurcation diagram of the system with s as the bifurcation parameter. We can see that there is a region of bistability, and as s decreases the cycle disappears in a homoclinic (saddle-loop) orbit. Now we can design the s dynamics in such a way that if a is small, s slowly increases, and when a is at higher values (as during the oscillation) s slowly decreases. Figure 22B shows the full model generating the rhythmic spontaneous activity.

5.3. Predictions of the model

The model predicts that a brief perturbation should bring the network from one steady state to the other, i.e. terminate or start an episode. Moreover, the bifurcation diagram in figure 22B predicts that if the perturbation is delivered early in the silent phase, then the following episode will be shorter, if the perturbation is delivered late in the silent phase the episode will be longer. This prediction has been confirmed experimentally [64]: there is a correlation between the time since the previous episode and the length of the next episode. The correlation

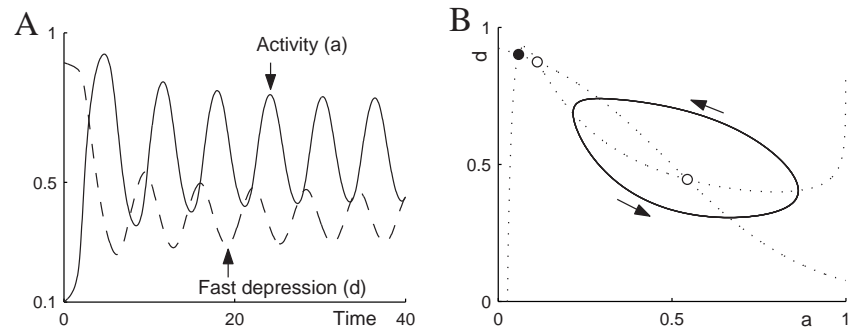


Fig. 21. Fast-subsystem of full model. *A*: Oscillations in $a - d$ subsystem with s frozen, $s = 0.9$. *B*: Oscillation can co-exist with a low-activity steady state (filled circle). It is shown here in the $a - d$ phase plane with $s = .78$.

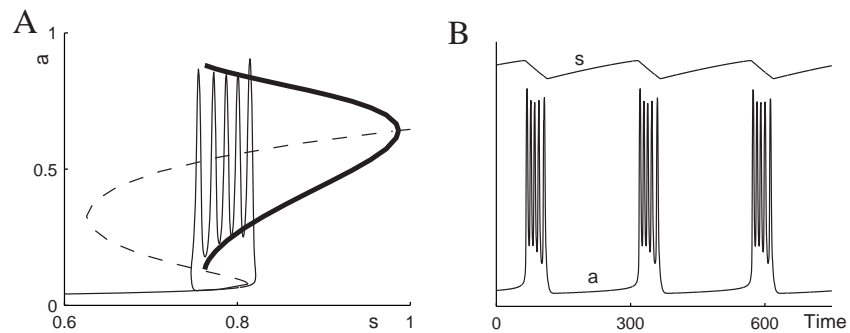


Fig. 22. *A*: Bifurcation diagram of the $a - d$ subsystem with s as a parameter. There is an S-shaped curve of the steady states (solid – stable, dashed – unstable), periodic orbits are shown with minimal and maximal a values (thick curve). Bursting solution of the full system is overlaid on top. *B*: Time courses of a and s of the same solution as in *A*.

is the same for both spontaneous and evoked episodes. This confirms that the termination of the episode is well-determined. On the other hand, no correlation has been found between the duration of the episode and the following silent interval, suggesting that stochastic effects influence episode initiation (for example, spontaneous synaptic release may cause some cells to fire, thereby triggering an episode).

The model also predicts the effects of pharmacological agents that alter the effective network connectivity. To do that we re-introduce the synaptic efficacy n :

$$\tau_a \dot{a} = a_\infty(n \cdot s \cdot d \cdot a) - a.$$

Synaptic blockers in the model have the effect of reducing n . Experimentally it was found that when some of the synapses are blocked, the network exhibits a prolonged silent phase and then settles into a slower rhythm (Fig. 23A). To explain this in the model let us call $\bar{s} = n \cdot s$. The fast subsystem is bistable over a particular range of \bar{s} values. If n is reduced the range of s in which oscillations exist moves to higher values of s . Therefore, just after n is decreased, initially the network must collapse to the silent state (as this is the only attractor at that value of \bar{s}). Before an episode can start s has to recover to a much higher value than before. This leads to a very prolonged first silent phase. Moreover, when s settles into its new range of operation the silent phase is now closer to the s -nullcline, which makes the rhythm's period longer.

The simulation of pharmacological manipulation of synapses was originally done to distinguish between a model that we just presented and one with a spike frequency adaptation instead of a synaptic depression s . The spike frequency adaptation model assumes that if a cell is active, then more and more input is needed to keep the activity at the same level. It is modeled by

$$a_\infty(input) = a_\infty(input - \theta),$$

and the threshold θ slowly increases with a :

$$\tau_\theta \dot{\theta} = \theta_\infty(a) - \theta.$$

It is found that for the θ -model, in contrast to the s -model the rhythm's period actually becomes shorter as connections are blocked and the length of each episode also significantly decreases (Fig. 23B). Experimental data agreed with predictions of the s -model. This favored synaptic depression as the proposed mechanisms for spontaneous rhythm generation in the embryonic spinal cord.

Recent experimental data [9] show that the reversal potential for Cl^- oscillates slowly in phase with the episodic rhythm. This variation contrasts with what is usually assumed, that for firing on short time scales the Nernst potentials for

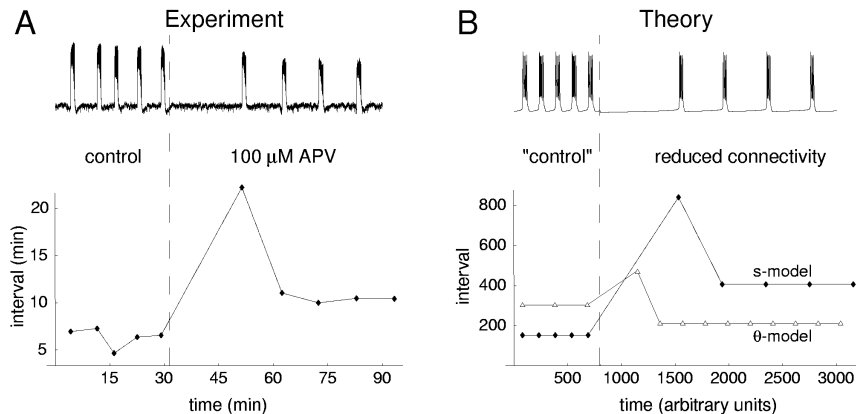


Fig. 23. Effect of a reduction of connectivity. *A*: Experimentally the connectivity is reduced by application of a synaptic blocker, NMDA-receptor antagonist, (adapted from Fig. 11 in [65]), after which there is one very long inter-event interval and then rhythm settles to a new (slower) period. *B*: Simulation results analogous to experiments in *A* for *s*-model and θ -model.

various ion species remain approximately constant. Such a slowly oscillating V_{Cl} could provide a specific mechanism for slowly modulating the GABA-mediated synaptic current, thereby a biophysical realization of the phenomenological *s*-variable in the model above. Thus, Cl^- handling dynamics have been introduced into the model (not shown here) as a specific mechanism for slowly modulating the GABA-mediated synaptic current. Synaptic activity and currents are strong during an episode leading to slow and considerable efflux of Cl^- . Consequently V_{Cl} slowly declines, making the GABA-synapses less "functionally excitatory", eventually terminating the episode. In the interepisode interval Cl^- efflux is very small and chloride pumps are able to slowly restore V_{Cl} so that a new episode can eventually begin.

6. Chapter summary

We have offered here an introduction to some concepts and techniques of dynamical systems theory that we and others have used to gain insight into neuronal dynamics. Our examples are illustrative of a variety of nonlinear behaviors including bifurcations, multi-stability, oscillations (tonic and bursting), and excitability primarily in the context of individual neurons. We have used reduced modeling formulations, fast-slow dissections, branch-tracking methods, phase plane geometrical treatments, stability analyses, and rapid equilibrium assump-

tions to gain insight into these behaviors. By applying these approaches to formulate and dissect a model of episodic rhythmicity in developing spinal cord you can see how one could analyze and understand mean field (firing rate) models for networks. We have restricted our attention to point models (non-distributed systems), neglecting the effects of cable properties of axons and dendrites at the cellular level and of spatial extension in networks of neurons. These latter considerations are important and mathematical treatments of the partial differential equations or integro-differential equations (say for networks, where cell coupling is handled by convolution integrals with kernels that represent synaptic weighting/footprints) involve the above and other techniques (some review is provided in [20]).

There are many other dynamical phenomena that we have not addressed including the effects of stochastic fluctuations, intrinsic to a cell or to synapses, or due to network sparseness and complex dynamical states (e.g., see [41, 44, 67]). We have focused on reduced models but yet have by-passed the historical literature having to do with non-continuous models like integrate-and-fire (see [67]) and modern, more general, formulations (e.g. [26]). We have not considered models of synaptic plasticity, in the sense of learning, which seem like natural candidates for fast-slow treatment.

We close by reiterating a primary take-home message: that in many of the continuous models excitability and oscillations are realized mechanistically by fast autocatalytic/regenerative processes and slower negative feedback. The former at the cell level are usually due to rapidly activating inward currents (due to Na^+ and/or Ca^{2+}) and the latter to slower activating outward currents (K^+) or slower inactivation of inward currents. At the network level recurrent excitation may be the autocatalytic process and synaptic depression is just one candidate for negative feedback.

6.1. Appendix A. Mathematical formulation of fast-slow dissection.

In order to describe the mathematical approach more systematically we imagine exaggerating the time scale differences in the Hodgkin-Huxley equations and introduce a "small" parameter ϵ to carry out this process. For simplicity we will again assume *a priori* that m is still much faster than V so that $m = m_\infty(V)$ is a valid idealization. Now, restating explicitly that V and m are fast relative to h and n we write the equations as follows:

$$\begin{aligned}\epsilon dV/dt &= [-I_{ion}(V, m_\infty(V), h, n) + I_{app}]/C_m, \\ dh/dt &= \phi [h_\infty(V) - h] / \tau_h(V), \\ dn/dt &= \phi [n_\infty(V) - n] / \tau_n(V).\end{aligned}$$

In this formulation if h and n vary on the time scale of msec then V (m as well) varies with an effective time constant of order ϵ . The upstroke and downstroke will occur very rapidly. In the limit, with ϵ very small, these phases appear almost as jumps. In order to describe these 2 fast phases (cf, Fig. 3A) we must stretch the time variable and look at the dynamics "inside" this time window. So we let, $s = t/\epsilon$ be the stretched time variable. Rewriting the equations in terms of s we get:

$$\begin{aligned} dV/ds &= [-I_{ion}(V, m_\infty(V), h, n) + I_{app}]/C_m, \\ dh/ds &= \epsilon\phi [h_\infty(V) - h]/\tau_h(V), \\ dn/ds &= \epsilon\phi [n_\infty(V) - n]/\tau_n(V). \end{aligned}$$

Now to get this "inner" solution we set $\epsilon = 0$ and find that, on the fast time scale, h and n are constant (say, equal to h_0, n_0 , respectively), according to the second pair of equations below:

$$\begin{aligned} dV/ds &= [-I_{ion}(V, m_\infty(V), h_0, n_0) + I_{app}]/C_m, \\ dh/ds &= 0, \\ dn/ds &= 0. \end{aligned}$$

This, of course, is just the mathematical expression of what we did for phases 1 and 3 in Section 2.3.2. With h_0, n_0 set to their resting values the equation for V is just the 1st order equation satisfied by the upstroke in this approximation when ϵ is small. Now to describe the solution during the plateau and recovery phases we look on the unstretched time scale, return to the first equation and set $\epsilon = 0$ there to get:

$$\begin{aligned} 0 &= -I_{ion}(V, m_\infty(V), h, n) + I_{app}, \\ dh/dt &= \phi [h_\infty(V) - h]/\tau_h(V), \\ dn/dt &= \phi [n_\infty(V) - n]/\tau_n(V). \end{aligned}$$

Here, V corresponds to an instantaneous crossing by $I_{inst}(V)$ of the level I_{app} , i.e. to a zero crossing of $I_{inst}(V)$ if $I_{app} = 0$. Of course there are in general, for the Hodgkin-Huxley equations, up to 3 such crossings (recall, R, T and E) and these V -values depend on h and n . Meanwhile h and n evolve according the 2nd and 3rd equations with, say during the plateau phase, $V = V_E(h, n)$. Geometrically, the first equation defines a surface in V, h, n space; a multi-valued and folded surface with (if V is the vertical direction) V_E the upper branch, V_R the lower branch, and V_T the middle branch. During the plateau the trajectory drifts along the surface's upper branch, until it reaches the "fold" where V_E and V_T coalesce. This is when the downstroke occurs. Then, because the trajectory leaves

the upper branch of the surface, we must revert to the fast time scale, stretch it, and capture the inner solution (the time course of V on the fast time scale of the downstroke) by switching to the fast equations with h, n held at their values when the fold is reached: $h = h_{down}$ and $n = n_{down}$. Then, having described the transition of V from the fold down to $V_R(h_{down}, n_{down})$, the trajectory drifts along the surface's lower branch according to the slow equation as the solution returns to rest, say if $I_{app} = 0$. If I_{app} is positive and large enough then the "rest" state does not lie on the lower surface but rather on the middle surface, in which case the trajectory reaches the knee of the lower surface and another upstroke occurs. This process continues, cycle after cycle, converging towards the periodic orbit of repetitive firing.

The procedure that we have described here is just the lowest order approximation to a series expansion of inner and outer solutions in the technique called matched asymptotic expansions (see, e.g. [37]).

6.2. Appendix B. Stability of periodic solutions.

Here we discuss how one can determine the stability and characterize bifurcations of the limit cycles. The idea is to reduce the problem to consideration of stability of a fixed point of a special map, called the Poincare map (see, for example [62, 71]). Let us first define this map. Suppose we have a system

$$\dot{x} = f(x) \tag{6.1}$$

and this system has a closed orbit (periodic solution) $p(t)$. Let us choose a plane S transversal to the vector field of the solutions in the neighborhood of a point p^* on the periodic solution $p(t)$, i.e. such that any solution that starts on the plane has to come out of the plane, not along it. Then consider the mapping P in the neighborhood of p^* in the plane defined in the following way. For every point x_0 consider the solution that starts at x_0 and trace it until it hits the plane again. The point x_1 at which the solution hits the plane is the image of x_0 under P : $x_1 = P(x_0)$. This map is the Poincare map. A closed orbit of the original system corresponds to a fixed point of the Poincare map: $p^* = P(p^*)$. Now we can consider its stability. Let us choose a small perturbation from the fixed point, such that it still lies in the plane S : $x = (p^* + v) \in S$, and then look at its image under P and the deviation of the image from p^* :

$$p^* + v_1 = P(p^* + v) = P(p^*) + [DP(p^*)]v + O(\|v^2\|),$$

where $DP(x)$ is the Jacobian matrix of P , called the linearized Poincare map. Remembering that $p^* = P(p^*)$, and using linear approximation, we see that

$$v_1 = [DP(p^*)]v.$$

The stability of the solution is now determined by the matrix $DP(p^*)$:

The closed orbit is linearly stable if and only if all eigenvalues σ_j of $DP(p^)$ satisfy $|\sigma_j| < 1$.*

Intuitively, the condition $|\sigma_j| < 1$ assures that at every iteration of P the deviation from the fixed point decreases. The quantities σ_j are called Floquet multipliers. Notice that P operates in the subspace transversal to the solution vector field. If one also considers perturbations along the periodic solution, for the autonomous system the corresponding eigenvalue will always be equal to 1. This is due to the time-invariance of the solutions of the autonomous system: a perturbation of the solution along the periodic orbit does not alter the solution. For more rigorous mathematical discussion the reader is referred to the dynamical systems literature, for example [10, 62, 71].

In practice $P(x)$ and $DP(x)$ are usually hard to compute. To avoid it, instead of considering the perturbed solutions on their return to S , one can consider the perturbed solutions at time T , where T is the period of $p(t)$ (see e.g. [10]). This gives a new mapping P' that takes a neighborhood of p^* in S to a surface S' which intersects with S at p^* . To characterize the linear approximation of P' we linearize the original equation 2.1 around $p(s)$:

$$\dot{x} = \left. \frac{\partial f}{\partial x} \right|_{p(s)} x,$$

then consider a set of solutions with initial conditions $X(0) = I$ (identity matrix), and their image under P' , $X(T)$. For stability of the point p^* and consequently the periodic solution $p(s)$, eigenvalues of $X(T)$ and of $DP(p^*)$ provide equivalent information under the same technical conditions that allow P to be well-defined.

Coming back to the Hodgkin-Huxley equations, let us write them in the form

$$\dot{y} = f(y; I_{app}),$$

where $y(t)$ corresponds to the column vector $(V, m, h, n)^t$ and assume that there is a periodic solution $p(t)$, stability of which we would like to compute. Linearize the equations around $p(t)$:

$$\dot{y} = \left. \frac{\partial f}{\partial y} \right|_{p(t)} y. \quad (6.2)$$

The Floquet multipliers can now be found by numerical integration of 6.2 with condition $Y(0) = I$ and computation of the four eigenvalues of $X(T)$. This was first done for the Hodgkin-Huxley equations in [57], where they also studied dependence of periodic solutions on temperature (see Section 2.4.2). It was also

shown [57] that for some parameter values (e.g. at temperature $Temp = 6.3^{\circ}\text{C}$) Floquet multipliers cross the unit disk at $\sigma = -1$, which gives birth to secondary (unstable) periodic orbits in a period-doubling bifurcation [71].

References

- [1] Adams W.B and Benson J.A. (1985) The generation and modulation of endogenous rhythmicity in the *Aplysia* bursting pacemaker neurone R15, *Prog. Biophys. Mol. Biol.*, 46: 1-49
- [2] Alving B. (1968) Spontaneous activity in isolated somata of *Aplysia* pacemaker neurons, *J. Gen. Physiol.*, 51: 29-45
- [3] Bertram R., Butte M.J., Kiemel T., and Sherman A. (1995) Topological and phenomenological classification of bursting oscillations, *Bull. Math. Bio.*, 57: 413-439
- [4] Booth V. and Rinzel J. (1995) A minimal, compartmental model for a dendritic origin of bistability of motoneuron firing patterns, *J. Comp. Neurosci.*, 2: 299-312
- [5] Butera R.J., Rinzel J., and Smith J.C. (1999) Models of respiratory rhythm generation in the pre-Botzinger complex: I. Bursting pacemaker neurons, *J. Neurophys.*, 82: 382-397
- [6] Canavier C.C., Clark J.W., and Byrne J.H. (1991) Simulation of the bursting activity of neuron R15 in *Aplysia*: role of ionic currents, calcium balance, and modulatory transmitters. *J. Neurophysiol.*, 66: 2107-2124
- [7] Chay T.R. and Keizer J. (1983) Minimal model for membrane oscillations in the pancreatic β -cell, *Biophys. J.*, 42: 181-190
- [8] Chub N. and O'Donovan M. (1998) Blockade and recovery of spontaneous rhythmic activity after application of neurotransmitter antagonists to spinal networks of the chick embryo. *J. Neurosci.*, 18: 294-306
- [9] Chub N. and O'Donovan M.J. (2001) Post-episode depression of GABAergic transmission in spinal neurons of the chick embryo. *J. Neurophysiol.*, 85: 2166-2176
- [10] Coddington E.A. and Levinson N. Theory of ordinary differential equations, McGraw-Hill, New York, 1955
- [11] Cole K.S., Guttman R., and Bezanilla F. (1970) Nerve excitation without threshold, *Proc. Nat. Acad. Sci.*, 65: 884-891
- [12] Connor J.A., Walter D. and McKown R. (1977) Neural repetitive firing: modifications of the Hodgkin-Huxley axon suggested by experimental results from crustacean axons, *Biophys. J.*, 18: 81-102
- [13] Connors B.W. and Gutnick M.J. (1990) Intrinsic firing patterns of diverse neocortical neurons, *Trends Neurosci.*, 13: 99-104
- [14] Cook L.D., Satin L.S., and Hopkins W.F. (1991) Pancreatic β -cells are bursting, but how?, *Trends Neurosci.*, 14: 411-414
- [15] Cooley J., Dodge F., and Cohen H. (1965) Digital computer solutions for excitable membrane models, *J. Cell Comp. Physiol.*, 66: 99-108
- [16] Del Negro, C. A., Hsiao, C.-F., Chandler, S. H., and Garfinkel, A. (1998) Evidence for a novel mechanism of bursting in rodent trigeminal neurons, *Biophys. J.*, 75: 174-82
- [17] Doiron B., Laing C., Longtin A., and Maler L. (2002) Ghostbursting: a novel neuronal burst mechanism, *J. Comp. Neurosci.*, 12: 5-25
- [18] Ermentrout B. Simulating, Analyzing, and Animating Dynamical Systems: A Guide to XPPAUT for Researchers and Students. SIAM, Philadelphia, 2002

- [19] Ermentrout B. (1998) Linearization of F-I curves by adaptation, *Neural Computation*, 10: 1721-1729
- [20] Ermentrout B. (1998) Neural networks as spatio-temporal pattern-forming systems, *Reports on progress in physics*, 61: 353-430
- [21] Fedirchuk B., Wenner P., Whelan P., Ho S., Tabak J., and O'Donovan M. (1999) Spontaneous network activity transiently depresses synaptic transmission in the embryonic chick spinal cord, *J. Neurosci.*, 19: 2102-2112
- [22] FitzHugh R. (1960) Thresholds and plateaus in the Hodgkin-Huxley nerve equations, *J. Gen. Physiol.*, 43: 867-896
- [23] FitzHugh R. (1961) Impulses and physiological states in models of nerve membrane, *Biophys. J.*, 1: 445-466
- [24] FitzHugh R. (1976) Anodal excitation in the Hodgkin-Huxley nerve model, *Biophys J.*, 16: 209-226
- [25] Galli L. and Maffei L. (1988) Spontaneous impulse activity of rat retinal ganglion cells in prenatal life, *Science*, 242: 90-91
- [26] Gerstner W. and Kistler W. *Spiking Neuron Models: Single Neurons, Populations, Plasticity.* Cambridge University Press, Cambridge, 2002.
- [27] Goldstein S.S. and Rall W. (1974) Changes of action potential shape and velocity for changing core conductor geometry, *Biophys. J.*, 14: 731-757
- [28] Golubitsky M., Josic K. and Kaper T.J. (2001) An unfolding theory approach to bursting in fast-slow systems. *In: Global Analysis of Dynamical Systems: Festschrift dedicated to Floris Takens on the occasion of his 60th birthday.* (H.W. Broer, B. Krauskopf and G. Vegter, eds.) Institute of Physics Publ.: 277-308
- [29] Gregory J.E., Harvey R.J., and Proske U. (1977) A late supernormal period in the recovery of excitability following an action potential in muscle spindle and tendon organ receptors and its effect on their responses near threshold for stretch, *J. Physiol.*, 271: 449-472
- [30] Guckenheimer J. and Holmes P. *Nonlinear Oscillations, Dynamical Systems, and Bifurcations of Vector Fields.* Springer Verlag, Berlin, 1990
- [31] Gutkin B.S. and Ermentrout G.B. (1998) Dynamics of membrane excitability determine interspike interval variability: a link between spike generation mechanisms and cortical spike train statistics, *Neural Computation*, 10: 1047-1065
- [32] Guttman R., Lewis S., and Rinzel J. (1980) Control of repetitive firing in squid axon membrane as a model for a neuroneoscillator, *J. Physiol. (Lond)*, 305: 377-395
- [33] Hille B. *Ion Channels of Excitable Membranes* (3rd Edition), Sinauer Associates, Sunderland, Mass., 2001
- [34] Hodgkin A.L. (1948) The local electric changes associated with repetitive action in a non-medullated axon, *J. Physiol. (London)*, 107: 165-181
- [35] Hodgkin A.L. and Huxley A.F. (1952) A quantitative description of membrane current and its application to conduction and excitation in nerve, *J. Physiol.-London*, 117: 500-544
- [36] Izhikevich E. (2000) Neural excitability, spiking and bursting, *Int. J. Bif. Chaos*, 10: 1171-1266
- [37] Keener J.P. *Principles of Applied Mathematics; Transformation and Approximation*, 2nd edition. Perseus Books, 1999.
- [38] Koch C. *Biophysics of Computation: Information Processing in Single Neurons.* Oxford University Press, New York, 1999
- [39] Llinas R.R. (1988) The intrinsic electrophysiological properties of mammalian neurons: insights into central nervous system function, *Science*, 242:1654-1664

- [40] Morris C. and Lecar H. (1981) Voltage oscillations in the barnacle giant muscle fiber, *Biophys. J.*, 35: 193-213
- [41] Nykamp D.Q., Tranchina D. (2000) A population density approach that facilitates large-scale modeling of neural networks: analysis and an application to orientation tuning, *J. Comput. Neurosci.*, 8: 19-50
- [42] O'Donovan M. (1999) The origin of spontaneous activity in developing networks of the vertebrate nervous system, *Curr. Opin. Neurobiol.*, 9: 94 -104
- [43] O'Donovan M. and Chub N. (1997) Population behavior and self-organization in the genesis of spontaneous rhythmic activity by developing spinal networks, *Semin. Cell Dev. Biol.*, 8: 21-28
- [44] Omurtag A., Knight B.W., Sirovich L. (2000) On the simulation of large populations of neurons, *J. Comput. Neurosci.*, 8: 51-63
- [45] Pinsky P.F. and Rinzel J. (1994) Intrinsic and network rhythmogenesis in a reduced Traub model for CA3 neurons, *J. Comp. Neurosci.*, 1: 39-60
- [46] Plant R.E. (1981) Bifurcation and resonance in a model for bursting nerve cells, *J. Math. Bio.*, 11: 15-32
- [47] Rall W. and Agmon-Snir H. (1998) Cable theory for dendritic neurons, *In: Methods in Neuronal Modeling: From Ions to Networks*, 2nd edition. (C. Koch and I. Segev, eds.), MIT Press, 27-92
- [48] Reyes A. (2001) Influence of dendritic conductances on the input-output properties of neurons, *Annu. Rev. Neurosci.*, 24: 653-675
- [49] Rinzel J. (1978) On repetitive activity in nerve, *Federation Proceedings*, 37: 2793-2802
- [50] Rinzel J. (1985) Bursting oscillations in an excitable membrane model. *In: Ordinary and Partial Differential Equations.* (Sleeman B.D. and Jarvis R.D., eds.) *Lecture Notes in Mathematics*, Springer, Berlin, 1151: 304-316
- [51] Rinzel J. (1987) A formal classification of bursting mechanisms in excitable systems. *In: Mathematical Topics in Population Biology, Morphogenesis, and Neurosciences* (E.Teramoto and M.Yamaguti, eds.), *Lecture Notes in Biomathematics*, Springer, Berlin, 71: 267-281
- [52] Rinzel J. (1990) Electrical excitability of cells, theory and experiment: review of the Hodgkin-Huxley foundation and an update. *In: Mangel M, ed. Classics of Theoretical Biology. Bull Math. Bio.*, 52: 5-23
- [53] Rinzel J. and Ermentrout B. (1998) Analysis of neural excitability and oscillations, *In: Methods in Neuronal Modeling: From Ions to Networks*, 2nd edition. (C. Koch and I. Segev, eds.), MIT Press, 251-291
- [54] Rinzel J. and Keener J.P. (1983) Hopf bifurcation to repetitive activity in nerve, *SIAM J. Appl. Math.*, 43: 907-922
- [55] Rinzel J. and Keller J.B. (1973) Traveling wave solutions of a nerve conduction equation, *Biophys. J.*, 13: 1313-1337
- [56] Rinzel J. and Lee Y.S. (1987) Dissection of a model for neuronal parabolic bursting, *J. Math. Biol.*, 25: 653-675
- [57] Rinzel J. and Miller R.N. (1980) Numerical calculation of stable and unstable periodic solutions to the Hodgkin-Huxley equations, *Math. Biosci.*, 49: 27-59
- [58] Rush M.E. and Rinzel J. (1995) The potassium A-current, low firing rates, and rebound excitation in Hodgkin-Huxley models, *Bull. Math. Biology*, 57: 899-929
- [59] Stafstrom C.E., Schwindt P.C., and Crill W.E. (1984) Repetitive firing in layer V neurons from cat neocortex in vitro, *J. Neurophysiol.*, 52: 264-277
- [60] Segev I. (1992) Single neurone models: oversimple, complex and reduced., *Trends Neurosci.*, 15: 414-421

- [61] Segev I. and London M. (2000) Untangling dendrites with quantitative models, *Science*, 290: 744-750
- [62] Strogatz S.H. *Nonlinear Dynamics and Chaos: With Applications to Physics, Biology, Chemistry, and Engineering*. Addison-Wesley, Reading, Mass., 1994
- [63] Strumwasser F. (1967) Types of information stored in single neurons. *In: Invertebrate Nervous Systems: Their Significance for Mammalian Neurophysiology* (C.A.G. Wiersma, ed.), The University of Chicago Press, Chicago, 290-319
- [64] Tabak J., Rinzel J., and O'Donovan M.J. (2001) The role of activity-dependent network depression in the expression and self-regulation of spontaneous activity in the developing spinal cord, *J. Neurosci.*, 21: 8966 - 8978
- [65] Tabak J., Senn W., O'Donovan M.J., and Rinzel J. (2000) Modeling of spontaneous activity in developing spinal cord using activity-dependent depression in an excitatory network, *J. Neurosci.*, 20: 3041 - 3056
- [66] Traub R., Wong. R., Miles. R., and Michelson H. (1991) A model of a CA3 hippocampal pyramidal neuron incorporating voltage-clamp data on intrinsic conductances, *J. Neurophysiol.*, 66: 635-649
- [67] Tuckwell H.C. *Introduction to Theoretical Neurobiology*. Cambridge Univ. Press, Cambridge, 1988, vol. 2.
- [68] de Vries G. (1998) Multiple bifurcations in a polynomial model of bursting oscillations, *J. Nonlin. Sci.*, 8: 281-316
- [69] Wang X.-J. (1993) Ionic basis for intrinsic 40 Hz neuronal oscillations. *Neuroreport* 5: 221-224
- [70] Wang X.-J. and Rinzel J. (1995) Oscillatory and bursting properties of neurons. *In: Handbook of Brain Theory and Neural Networks*, edited by M. Arbib, MIT Press, 686-691
- [71] Wiggins S. *Introduction to Applied Nonlinear Dynamical Systems and Chaos*, Springer Verlag, Berlin, 1990
- [72] Wilson H.R. and Cowan J.D. (1972) Excitatory and inhibitory interactions in localized populations of model neurons, *Biophys. J.*, 12: 1-24